This is a non-peer-reviewed preprint submitted to EarthArXiv.

Transient liquid- and solid-dominated inflation of an upper crustal magma chamber: insights from the Carlingford Complex (Ireland)

Beckwith, J.[1*], Stock, M.J.[1], Holness, M.B.[2], Cooper, M.R.[3], Andersen, J.C.Ø.[4], Huber, C.[5], Chew, D.M.[1], Higgins, O.[6,7], Carter, E.J.[1,8], Broom-Fendley, S.[4]

[1] Discipline of Geology, School of Natural Sciences, Trinity College Dublin, Dublin, Ireland

[2] Department of Earth Sciences, University of Cambridge, Cambridge, United Kingdom

[3] Geological Survey of Northern Ireland, British Geological Survey, Belfast, United Kingdom

[4] Camborne School of Mines, University of Exeter, Penryn, United Kingdom

[5] Department of Earth, Environmental, and Planetary Sciences, Brown University, Providence, United States

[6] School of Earth and Environmental Sciences, University of St. Andrews, St. Andrews, United Kingdom

[7] Department of Earth and Environmental Sciences, The University of Manchester, Manchester, United Kingdom

[8] Department of Geography, Geology, and the Environment, Keele University, Keele, United Kingdom

*Corresponding author: Jack Beckwith (beckwitj@tcd.ie)

ABSTRACT

Layered intrusions are the crystallised remnants of magma reservoirs and preserve a detailed record of magma storage, differentiation, and recharge processes in the upper crust. Their assembly is commonly categorised into two end-member emplacement regimes: long-lived liquid-dominated magma chambers, and incrementally assembled crystal-rich mush systems. These end-members are often presented as competing concepts despite intrusions necessarily spanning a range of crystal fractions as they cool and crystallise. The Carlingford Complex (Co. Louth, Ireland) preserves the shallow-crustal architecture of a volcanic centre emplaced during plume-related rifting of the North Atlantic, thus providing the opportunity to evaluate contrasting models of subvolcanic magma reservoir assembly. Integrated field observations, microstructural analysis, mineral and bulk-rock geochemistry define four stratigraphic zones that record systematic changes in emplacement behaviour. High-resolution sampling of outcrop and drill core material reveals a previously unrecognised Lower Zone that extends the intrusion downward and represents its most mafic portion, preserving evidence for pulsed replenishment and accumulation within an open, liquid-dominated environment. The overlying Middle Zone marks the transition to a phase of high melt flux in a largely closed system, with microstructural and geochemical trends indicating intrusion-scale crystal settling, flotation, and convection. Upper Zone A records chaotic emplacement of multiple, laterally discontinuous sills in an open, crystal-rich environment. Upper Zone B mirrors the geochemical trends of the Middle Zone but is locally disrupted by small-scale sills and microstructures consistent with late-stage fluid infiltration. Together, these variegated petrological zones provide compelling evidence that subvolcanic systems can alternate between liquid- and crystal-dominated emplacement regimes over relatively short spatial and temporal intervals, highlighting their sensitivity to changes in melt flux and thermal state. These findings have direct implications for understanding magma supply to volcanoes and the formation of associated mineral deposits.

INTRODUCTION

Mafic-ultramafic intrusions provide insight into the emplacement dynamics of upper-crustal magma reservoirs and are increasingly conceptualised through two competing end-member models (Cawthorn, 2012; Edmonds *et al.*, 2019; Holness *et al*., 2019; Sparks *et al.*, 2019; Humphreys *et al*., 2025). For over a century, crustal magma system assembly has been envisaged through a paradigm of liquid-dominated 'magma chambers' whereby differentiation is driven by gravity-driven accumulation and flotation of crystals on the chamber floor and roof, respectively (Wager & Brown, 1968; Irvine, 1970, 1980; Marsh, 1996). In recent decades, however, studies have tended towards an alternative 'mush model', whereby magmas stored in the crust predominantly comprise zones of crystal-rich material, formed through multiple low-volume intrusions (Hildreth, 2004; Bachmann & Bergantz, 2004; Marsh, 2004). Although often presented as dichotomous (Mungall *et al*., 2016; Cashman *et al*., 2017; Jackson *et al*., 2018), these end-member models are intrinsically linked through magma cooling and crystallisation histories and can instead be viewed as forming an evolutionary continuum: intrusions are initially emplaced under melt-rich conditions and progressively evolve toward more crystal-rich, prolonged mushy states as cooling rate decreases with increasing crystallinity (Huber *et al.*, 2009). Constraining how this evolution progresses in natural systems is central to addressing fundamental questions of crustal development (Rudnick *et al*.., 1995; Scoates & Wall, 2015; Roman & Jaupart, 2016), volcanic eruption triggering (Nakagawa *et al*., 2002; Neave *et al*., 2017; Higgins *et al*., 2025), and enrichment of economically important metals (O'Driscoll & VanTongeren, 2017; Latypov *et al.*, 2022).

The shift towards mush-based models of magma storage is underpinned by geophysical observations which attest to low melt fractions in active volcanic systems (Paulatto *et al*., 2012; Ward *et al.*, 2014; Huang *et al*., 2015), as well as petrological evidence for complex crystal cargos with distinct growth histories (Nakagawa *et al*., 2002; Neave *et al.*, 2017; Maclennan, 2019; Stock *et al*., 2020) short lifetimes of melt-rich bodies (Cooper, 2019; Jollands *et al.*,

2020), and out-of-sequence stratigraphies (Mungall *et al.*, 2016, Wall *et al.*, 2018). It is, however, contentious and cannot always reconcile large-scale stratigraphic trends in geochemistry (Nielsen, 2004; Latypov *et al.*, 2022) or microstructural observations (Holness *et al.*, 2019; Vukmanovic *et al.*, 2018). Further, the validity seismic imaging methods in estimating melt fractions has been recently brought into question (Lees, 2007; Paulatto *et al*., 2022; Huber *et al*., 2025a). The dichotomous framing of magma chamber emplacement models (Mungall *et al*., 2016; Cashman *et al*., 2017; Jackson *et al*., 2018) is particularly challenging in the context of large, economically significant (i.e., metal-rich) intrusions where contrasting interpretations underpin competing models for ore formation. For example, the Bushveld Rustenburg Layered Suite has conventionally been interpreted as the product of a long-lived liquid-dominated magma chamber with an internal structure controlled by mechanical processes (i.e. crystal flotation, settling and convection; Wager & Brown, 1968; Latypov *et al.*, 2022) and reef-style mineralisation (Kruger, 2005), but has more recently been argued to have formed by the incremental assembly of crystal-rich sills (Mungall *et al.*, 2016; Yao *et al.*, 2021), lending to more complex models of ore formation involving reactive percolating fluids (Boudreau & McCallum, 1992).

The well-preserved and exposed intrusions associated with the North Atlantic Igneous Province (NAIP) formed between 62 and 58 Ma (Saunders *et al.*, 1997; Wilkinson *et al*., 2017), during the early phase of rifting triggered by the arrival of the proto-Icelandic plume at the base of the lithosphere. These intrusions were the basis for work that laid the foundation for core concepts in igneous petrology (e.g., Skaergaard; Wager & Deer, 1939) and provide excellent case studies for testing the relevance of magma system emplacement models. The Skaergaard Intrusion, for example, is widely regarded as an archetypal liquid-dominated system which was emplaced rapidly with the history of fractionation recorded by systematic, large-scale geochemical and mineralogical trends (Wager & Deer, 1939; Wager & Brown, 1968; McBirney & Noyes, 1979). In contrast, the Rum Eastern Layered Intrusion formed through incremental inflation of

multiple sill-like bodies in a mushy environment, as evidenced by geochemical and microstructural reversals (Holness & Winpenny, 2008; Holness *et al.*, 2007a), and field evidence of morphologically complex and laterally discontinuous layers (Hepworth *et al.*, 2017).

In this contribution, we use the gabbroic Carlingford Complex, part of the British Irish Paleogene Igneous Province (BIPIP) component of the NAIP (Fig. 1a), as a natural laboratory to interrogate the processes of crustal magma system assembly. The complex has exceptional preservation of a shallow-crustal magmatic stratigraphy, which provides insights into the physical and chemical processes operating through magma storage system, linked to surface volcanism. Our integrated approach combines bulk-rock geochemistry, *in situ* mineral analyses and petrographic observations to provide first-order constraints on the primary magmatic processes responsible for their formation. Through comprehensive stratigraphic characterisation of the Carlingford layered gabbros, we show that its complex emplacement history is inconsistent with either a discrete liquid- or mush-based model, instead involving multiple transitions between these regimes resulting from changes in the incoming magma flux (and therefore magma system temperature).

GEOLOGICAL BACKGROUND

The Carlingford Complex, Co. Louth, Ireland, is a bimodal body comprising a granitic ring-dyke and gabbros, cut by later dolerite cone sheets. Proximal basaltic lavas and vent agglomerates indicate that the intrusive components formed part of a shallow magmatic system feeding an overlying active volcanic centre. The subject of intense petrological study in the 19th and 20th centuries, the Carlingford Complex informed contemporary ideas of magma system development (Richey, 1932), magma mixing and mingling (Nockolds, 1935; Nockolds & Mitchell, 1944), and metamorphism and metasomatism (Osborne, 1932; Nockolds &

Vincent, 1947). Evidence of sulphide mineralisation prompted exploration drilling in the 1970s (Hurst, 1997; Buchanan, 2012), although subsequent academic investigation is limited.

Like the NAIP, reliable geochronological constraints for Carlingford, and its neighbouring Slieve Gullion and Mourne Mountains central complexes in Northern Ireland (Cooper *et al.*, 2004) (Fig. 1a, 1b), are scarce (Wilkinson *et al.*, 2017). However, a U-Pb SHRIMP age of 61.4 Ma ± 0.8 Ma for a microgranite from the Carlingford Complex (Mitchell *et al.*, 1999) suggests that there was magmatism here during extrusion of the Lower Basalt Formation of the Antrim Lava Group (Cooper, 2004). Furthermore, a suite of U-Pb TIMS ages for the Paleogene rocks of Northern Ireland and the north of Ireland (Cooper *et al.*, 2020) indicate that the adjacent Slieve Gullion Complex was active c. 60.8-60.7 Ma, which is slightly younger than the Carlingford age constraints for the Lower Basalt Formation at c. 61.6-61.1 Ma. Evidence from isotopic dating, and from Tellus Project airborne geophysical survey datasets (Young & Donald, 2013; Hodgson & Young, 2016), indicate that both centres experienced multiple episodes of magmatism during the Paleocene, though further work is needed to fully decipher the history of magmatism in this region.

Consequently, the relative timing of the Carlingford microgranites and the gabbros remains a subject of contention. Based on field relations, it has been argued both that the gabbros pre-date the microgranite (Griffith, 1840; Sollas, 1892; Richey, 1932; Le Bas, 1967), and that the gabbros post-date the microgranite (Lasaulx, 1878; Bailey, 1961; De & Poole, 1974; O'Driscoll, 2006) (Fig. 2). Bulk-rock radiogenic isotope dating of both units using K-Ar (Evans *et al.*, 1973), $^{40}Ar/^{39}Ar$ (Thompson, 1985), and Rb-Sr (O'Connor, 1990) systems provides little clarity, with the reliability of results questioned based on later hydrous alteration (Mussett *et al.*, 1988), assimilation (O'Connor, 1990), and remelting. Recent work using detailed Sr, Nd, and Pb isotopic analyses resulted in a model termed ‘progressively inhibited crustal assimilation’, whereby the microgranites were produced by high-volume melting of crustal

metasediments, with waning temperatures restricting assimilation to increasingly refractory compositions, permitting the eventual emplacement of mafic magmas (Meade *et al.*, 2014).

The Carlingford gabbros were first described by Le Bas (1960), who divided them into the 'Early Gabbros', exhibiting alkaline affinities (Charlesworth, 1960), and the tholeiitic 'Later Gabbros'. Confined to Trumpet Hill (Fig. 1b), the Early Gabbros have received no subsequent attention. Le Bas (1960) argued that the Later Gabbros comprise a lopolithic sheet with an undulose base dipping (>0–50°) towards the centre of the complex (Fig. 2). This model was based on observations of meter-scale joint surfaces which occur throughout the complex, which strike radially and dip inward, and was later supported by magnetic fabric data consistent with central subsidence (O'Driscoll, 2006). Le Bas (1960) divided the Later Gabbros into four layers, shorthanded as E1-E4, with the base of E1 at the stratigraphically lowest surface exposure, and E4 representing the uppermost exposures: the top of E4 is not preserved. The complete sequence is exposed only at Slieve Foye, but is locally offset by faulting, including the Two-Mile Fault (Fig. 1c). Le Bas's (1960) subdivisions were defined using optically determined mineral compositions and on basal enrichment in modal olivine and were based on samples collected from outcrops without stratigraphic control. Subsequent bulk-rock compositions and mineral trace-element chemistry determined by semi-quantitative spectrographic analysis revealed broad fractionation trends, including progressive SiO_2 enrichment of gabbros up-stratigraphy alongside decreasing olivine Fo contents (Le Bas, 1970).

Dolerite cone sheets cut all major intrusive units at Carlingford (Fig. 3a). They commonly contain abundant plagioclase phenocrysts, either as isolated grains or as clusters with clinopyroxene: many of the sheets show a central concentration of the plagioclase cargo, due to flow sorting (the Bagnold effect; Bagnold, 1954) (Fig. 3b). The cone sheets are radially distributed, dipping towards a central focus beneath the complex (Halsall, 1974, Schauroth *et al.*, 2014). The presence of a gravitational Bouguer anomaly from 2–3 km beneath the complex

and extending to ~10 km depth (Cook & Murphy, 1952), suggests that the cone sheets may be a useful tool to constrain the deeper architecture of the complex, though structural and geobarometric depth estimates using the sheets are associated with large uncertainties (Halsall, 1974; Meade *et al.*, 2014).

SAMPLING STRATEGY

Building on Le Bas's (1960) initial characterisation, we targeted North Foye and Southeast Foye to collect broadly linear transects through the stratigraphy of the Carlingford Later Gabbros (Fig. 1c). Sampling positions were determined by GPS, digital elevation model (DEM) data, and field observations; unit boundaries were remapped following Le Bas's (1960) units and refined where necessary based on our field data. True stratigraphic heights were obtained using averaged strike and dip measurements for each transect, with the base of layer E1 representing a nominal height of 0 m. Samples from the upthrown block north of the Two-Mile Fault were stratigraphically corrected to the southern block in the North Foye transect using the E3–E4 stratigraphic boundary defined by Le Bas (1960). To ensure representative bulk analysis, material was sampled to yield a post-processed mass >500 g.

The North Foye transect spans the thickest exposure, from the base of unit E1 to the top of E4, the only locality where E4 is found. The Southeast Foye transect encompasses Le Bas's E1 to E3, serving to assess the lateral continuity of the gabbros. The most extensive drill core intersecting the gabbros was targeted for a third transect, extending vertically 120 m beneath the base of E1 at the southern flank of Slieve Foye, permitting sampling of material not available to Le Bas. Sampling of the core was guided by the original stratigraphic log (Mulligan, 1983), targeting lithological boundaries where present and an average sample spacing of ~3 m elsewhere. Forty-centimetre lengths of half-core material were taken to obtain ~ 500 g for representative analysis.

ANALYTICAL METHODS

Sample preparation

Samples of fresh gabbro were prepared in the Discipline of Geology, Trinity College Dublin. Hand samples were cut to remove all visible surface weathering, alteration, and veins using a circular diamond-tipped rock saw with significantly altered samples discarded. Representative billets were set aside for thin sectioning. Approximately 500 g of cleaned sample were dried at 60 °C for 24 hours and crushed to < 2 mm using a tungsten carbide Jaw Crusher. Sixty-gram aliquots were then powered to < 30 μm using a TEMA disk mill with an agate grinding vessel.

A total of 110 samples were prepared for bulk-rock geochemical analysis and thin sections for qualitative petrography. Of these, 75 samples distributed throughout the stratigraphy were point counted to quantify modal mineralogy, 51 were measured for clinopyroxene-plagioclase-plagioclase dihedral angles, and 25 were selected for *in situ* electron probe microanalysis (EPMA). Olivine grain shape parameters were quantified from a subset of 13 samples.

Petrography

Representative thin sections were scanned at high resolution in plane and cross polarised transmitted light using a Nikon DS-Ri2 camera-mounted Nikon Eclipse LV100 microscope, before creating full-section electron backscatter (BSE) scans using a TESCAN scanning electron microscope, both in the Centre of Microscopic Analysis, Trinity College Dublin.

Microstructural observations were complemented by quantitative modal analysis, determined via random grid point counting, using the software JMicroVision (Roduit, 2007). Samples with >15 vol.% alteration in thin section were not analysed for mineral modes. Where thin section coverage of drill core samples was limited, CIPW normative mineral abundances are reported as an alternative, calculated using shinyNORRRM (González-Guzmán *et al.*, 2023). See Supplementary Fig. S1 for a comparison of measured modal vs calculated normative abundances.

Size and shape data for olivine grains were obtained by tracing outlines of individual grains in a whole BSE thin-section scan, discarding grains truncated by section edges and alteration veins. Shape data were quantified using ImageJ (Schneider *et al.*, 2012), using the 'Analyse Particles' function set with a known scale.

Dihedral angles at clinopyroxene-plagioclase-plagioclase three-grain junctions were measured using a 4-axis Leitz universal stage mounted on a James Swift monocular microscope fitted with a UM32 Leitz long-working-distance objective and 10-times magnification eyepiece in the Department of Earth Sciences, University of Cambridge. Dihedral angles provide quantitative constraints on the thermal history of magmatic systems, as the geometry of three-grain junctions involving two grains of plagioclase reflects cooling and solidification rates: in fractionating systems, this is a function of liquid phase assemblage via the control by the fraction of the overall heat loss provided by latent heat release (Holness *et al.*, 2013). For each section, >30 true 3D angles were measured to obtain the median value, Θ_{cpp}: 95% confidence intervals around the median were calculated following Stickels and Hücke (1964).

Bulk-rock chemistry

Powdered samples were made into fused glass beads and pressed powder pellets for major- and trace-element analysis using a Panalytical Zetium Wavelength Dispersive X-ray Fluorescence Spectrometer (WD-XRF) in the Earth Surface Research Laboratory, Trinity College Dublin, respectively. This is with the exception of 22 fused glass beads analysed for major elements using a Panalytical Zetium WD-XRF in the Malvern Panalytical Laboratory, Nottingham (indicated in Supplementary Table S1). Sample preparation and analysis were conducted following Carter *et al.* (2024), with samples ignited for two hours at 1000 °C in a SNOL muffle furnace for loss on ignition (LOI) determinations. Analytical accuracy and precision are based on laboratory analysis of representative reference materials are in Supplementary Table S1.

Mineral chemistry

Core, mantle, and rim measurements were made on olivine, clinopyroxene, and plagioclase grains using a JEOL JX-8200 electron-probe at Camborne School of Mines, University of Exeter. All analyses were collected using a 15 nA, 15 kV defocused (5 μm) beam. Measurements were internally calibrated using appropriate AST and MK2 primary standards, with peak count times 10-25s, extended to 40s for Na_2O, and backgrounds measured for half of the on-peak time either side of the peak. Repeat analyses of compositionally similar secondary standards are accurate within ±4% of reported values for major elements, with 1σ analytical precisions better than ±2%. Minor elements were typically accurate within ±15%, with 1σ precisions better than ±7%. Exceptions include Na_2O in clinopyroxene (±17% accuracy; ±11% precision) and FeO in plagioclase (±20% accuracy). Full analytical conditions and uncertainties are provided in Supplementary Table S2.

RESULTS

Field Observations

We observed interactions between the felsic and mafic units of the Carlingford Complex at three localities. In Cooley Castle Quarry, dolerite is net-veined by silicic rock (Fig. 3e) and locally forms pillows with lobate, fine-grained margins (Fig. 3f) in contact with coarser-grained microgranite (*sensu lato*). On the southern flank of Slieve Foye, microgranitic/aplitic net veining in the gabbro is present (Supplementary Fig. S2). The basal 5 m of the drill core comprises microgranite, separated from the overlying gabbro by a diffuse contact: this lower part of the core also cuts ~1 m of partially hybridised dolerite. Structural measurements of layering surfaces at both the North and Southeast Foye transects give strike orientations broadly concordant with topographic contours, dipping approximately southwest towards the centre of the complex with a mean dip of 34° and 33° respectively (Fig. 1; Supplementary Table S3).

Our work has resulted in a revised stratigraphy for the layered gabbros, which are divided into the Lower (LZ), Middle (MZ) and Upper Zones: The Upper Zone is further subdivided into

Upper Zone A (UZA) and Upper Zone B (UZB). While the LZ comprises material not described by Le Bas (1960), the MZ comprises units E1 and E2, while UZA equates to E3, and UZB to E4 (see Table 1 for a summary of layer equivalencies). Three samples belonging to the Lower Zone were identified in outcrop; however, their stratigraphic positions are ambiguous. Accordingly, LZ stratigraphic trends are described using drill core material unless otherwise stated. Results are presented in stratigraphic order, from base to top.

Petrographic observations

In order of average abundance, the gabbros comprise plagioclase, clinopyroxene, and olivine, with minor oxides and sulphides (Fig. 4; Supplementary Fig. S1). Olivine is commonly serpentinised, with local development of iddingsite towards the base of the intrusion, and clinopyroxene is also locally replaced by chlorite or amphibole. Rare anorthosites are present at the top of the intrusion (within UZB). Median Θ_{cpp} is primarily bimodal throughout the intrusion, with values of either ~97˚ or ~87˚ (Fig. 5). Full quantitative petrographic datasets are provided in Supplementary Table S4.

Lower Zone (LZ)

The LZ represents the most olivine-rich unit within the layered gabbros. Modal mineral abundances (Fig. 6) show olivine contents ranging from 11.2% to 45.5% (mean 21.2%). Plagioclase mode ranges from 36.1% to 70.1% (mean 60.8%). Clinopyroxene forms cm-scale oikocrysts, enclosing plagioclase and olivine (Fig. 7a) throughout the LZ, with a mode ranging from ~7.1 to 23.5% (mean 14.2%).

The LZ comprises cyclic units, numbered C1 to C11, characterised by relatively olivine- and clinopyroxene-rich bases in which olivine typically forms idiomorphic, rounded grains that are commonly clustered (Fig. 7a). Clinopyroxenes are intercumulus, whilst plagioclase predominantly occurs as fine-grained, randomly oriented grains with an apparent aspect ratio of ~2, though some larger, lower aspect ratio, grains are also present. Towards the top of each

cyclic unit, plagioclase increases in abundance at the expense of olivine and clinopyroxene, reaching modes of up to 70.9%. On average, modal variations from base to top of each cyclic unit record relative changes of ~25% increase in olivine, ~46% increase in clinopyroxene, and ~15% decrease in plagioclase. This upward progression is accompanied by a transition towards fewer, larger, anhedral olivines, a lower volume of intercumulus clinopyroxene, and a change in shape of plagioclase grains to an aspect ratio of ~1 (Fig. 7b).

There is a shift from higher (~97°) to lower (87°) values of Θ_{cpp} between cyclic units C6 and C9 (Fig. 5), which is not accompanied by a discernible change in clinopyroxene habit. At North Foye, low Θ_{cpp} are found in the single LZ sample analysed (-7.6 m; sample 22CCCI3-16). In contrast, the LZ exposed in Southeast Foye has high median Θ_{cpp} despite the lower value being expected at this point in the stratigraphy on the basis of dihedral angle trends from the core (Fig. 5).

Middle Zone (MZ)

The base of the MZ is characterised by the abrupt appearance of abundant, compact, euhedral clinopyroxenes, locally displaying simple twinning (Fig. 7c), defining an adcumulate texture. Locally, clinopyroxene forms highly irregular crystals suggestive of an early stage of dendritic growth, though with no clear evidence of directional growth, perhaps associated with temporary oversaturation of the bulk magma in clinopyroxene (Fig. 8). The addition of clinopyroxene to the liquidus assemblage is associated with the median Θ_{cpp} switching to the higher of the bimodal values (~97°), where it remains throughout the MZ. Plagioclase locally forms clusters (Supplementary Fig. S3).

The lower portion of the MZ is characterised by rhythmic modal layering, commonly accentuated by weathering. Layers are typically 10s of cm thick and are either planar or trough-shaped (Fig. 3c). Higher in the MZ, the gabbros have a more orthocumulate texture, with primocrysts displaying progressively greater amounts of interstitial overgrowth. The olivine

mode decreases upwards through the MZ, reaching zero in some horizons (Fig. 4); the clinopyroxene mode also decreases, associated with the development of extensive, normally zoned interstitial overgrowth, coarsening in size towards the intrusion centre. Plagioclase becomes more modally dominant, progressively coarser, and with a lower aspect ratio, towards the top of the MZ (Fig. 7d).

The trends in microstructural evolution broadly correlate between North and Southeast Foye, though the variability in olivine enrichment at the base of the MZ may reflect natural heterogeneity or stratigraphic uncertainty between transects.

Upper Zone A (UZA)

The Upper Zone (both UZA and UZB) is characterised by sharply-defined modal layering (Fig. 3d). Unlike the systematic stratigraphic variations through the LZ and MZ, the microstructures and modal mineralogy of UZA vary both laterally and stratigraphically.

At North Foye, the base of UZA is marked by the reappearance of abundant aggregates of euhedral clinopyroxene, together with idiomorphic olivine, fine-grained plagioclase, and occasional large, low aspect ratio, plagioclase crystals (Fig. 9a). Clinopyroxene is a cumulus phase throughout this transect at UZA, though in varying proportions and grain size. The gabbros are rarely foliated. Notably, the thin section for sample 22CCCI3-21 (407.5 m) captures a strong alignment of fine-grained, high aspect ratio plagioclase laths in irregular contact with the surrounding coarse gabbro (Fig. 9b).

In contrast, the base of UZA at Southeast Foye is marked by the abrupt appearance of poikilitic clinopyroxene enclosing plagioclase with or without olivine, though with higher average pyroxene mode than the poikilitic LZ gabbros (Fig. 9c). While pyroxene remains apparently interstitial through much of UZA at Southeast Foye, a primocrystic habit is present locally, with rare examples of isolated, rounded pyroxene grains enclosed by plagioclase (Fig. 9d).

This contrast in clinopyroxene habit correlates with Θ_{cpp}: values are generally ~97˚ at North Foye (with the exception of 22CCCI3-21) whereas at Southeast Foye, values oscillate between ~97˚ in those samples with clinopyroxene primocrysts, and ~87˚ in those with clinopyroxene oikocrysts. There are, however, some exceptions, with some poikilitic gabbros recording the higher median value of Θ_{cpp} (e.g., 22CCCI5-07; 368.9 m).

Upper Zone B (UZB)

UZB is exposed only in North Foye, with its base marked by a distinctive adcumulate rich in olivine and pyroxene primocrysts reminiscent of the base of UZA at North Foye (Fig. 9e). The UZB adcumulate is relatively coarse-grained, with well-developed clusters and chains of the pyroxene primocrysts. Higher in UZB, the plagioclase mode increases in an irregular manner, reaching anorthositic compositions towards the top of the unit (Fig. 9f). At ~500 m, a decline in clinopyroxene mode is accompanied by a shift from cumulus to interstitial clinopyroxene, proceeded by a modal increase in subhedral olivine. In contrast to the other units, in which Θ_{cpp} is highly bimodal, Θ_{cpp} in UZB gradually decreases from high to low values between 440 m to 465 m.

Bulk-rock chemistry

Bulk-rock geochemistry provides the most effective means of distinguishing the zonal variations through stratigraphy and for evaluating parity along-strike. The majority of analysed samples are tholeiitic gabbros, with some picrogabbros occurring in the LZ (Supplementary Fig. S4). Major- and trace-element geochemistry for all samples in this study are reported in Supplementary Table S1.

The LZ is characterised by low Ti concentrations (mean 0.19 wt.%), low CaO/Al_2O_3 (mean 0.63), elevated Ni contents (up to 585.7 ppm), and the highest MgO values (up to 22.2 wt.%) of the layered gabbros (Fig. 11). The bases of cyclic units are marked by enrichments in Cr_2O_3 and MgO, together with relatively high values of CaO/Al_2O_3. This is often accompanied by

increases in Ni and FeO, and an upward increase in Al_2O_3 and Sr (Fig. 11). Strontium broadly decreases with stratigraphic height. Superimposed on these trends within each subunit is a broader compositional change at the boundary between subunits C6 and C7, characterised by a general reduction in Cr_2O_3 concentrations and a general increase in Ni and MgO concentrations (Fig. 11).

The base of the MZ is characterised by sharp increases in TiO_2 (0.50 wt.%) and CaO/Al_2O_3 (1.61) (Fig. 10), which decrease steadily up through the lower ~100 m of the MZ, together with Ni and Mg# (molar $Mg/[Mg+Fe^{2+}+Fe^{3+}]$). The concentration of Sr shows the inverse behaviour.

UZA is distinguished by geochemical excursions away from the gradual up-section variation observed in the MZ, though no clear stratigraphic trends are evident in either North or Southeast Foye. Rather, major-element compositions fluctuate over a similar compositional range as in the MZ (Fig. 10). Southeast Foye has lower average CaO/Al_2O_3 ratios than North Foye.

UZB is marked by a basal increase in Ni and Mg#, followed by a sharp increase in TiO_2 and CaO/Al_2O_3 (Fig. 10). Concentrations of these elements decline steeply through the overlying ~100 m, with Mg# reaching the lowest values observed anywhere in the intrusion (46.1 mol.%), and display a reversal in the upper 25 m. This general trend is disrupted by sample 22CCCI3-37 (447.8 m), which records lower MgO and higher Al_2O_3 than surrounding samples, and by sample 22CCCI3-33 (494.0 m), which shows the opposite relationship. A compositional gap is present at ~450 m for both Al_2O_3 (16.0 to 23.3 wt.%) and MgO (9.3 to 5.2 wt.%) values, despite close sample spacing.

Mineral chemistry

Clinopyroxene in the Carlingford Later Gabbros straddles the diopside–augite fields (Supplementary Fig. S5) and exhibits normal zoning toward the grain margins, irrespective of whether they are cumulus or intercumulus (Fig. 12). Olivine grains are unzoned, while normal

zoning in plagioclase varies in magnitude throughout the intrusion (Fig. 13). Mineral compositions reported below refer to median core compositions calculated per sample, unless otherwise stated. Full EPMA mineral analyses are reported in Supplementary Table S5.

The highest forsterite (Fo = Mg/[Mg+Fe^{2+}] on a molar basis) contents of olivine are found in the LZ, where olivine remains consistently forsteritic (zone mean Fo_{74}; Fig. 13). Plagioclase cores become progressively more anorthitic up-sequence (An_{79} to An_{84}) with the smallest relative core-rim compositional variation of any zone (-1.7%). Clinopyroxene cores grade towards lower CaO compositions up-sequence through the LZ (22.0 to 21.5 wt.%), with several samples showing a rimward increase in CaO that is not observed elsewhere in the intrusion (Fig. 13).

A stepwise decrease in olivine Fo occurs at the LZ–MZ boundary (Fo_{75} to $Fo_{68;}$ Fig. 13), followed by a slower upwards reduction through the MZ (to Fo_{65}). Plagioclase An contents show a comparable decrease at the boundary but subsequently increase up-sequence (An_{74} to An_{83}) and cover a wider compositional range than in the LZ. Clinopyroxene CaO compositions are lowest in the central outcrops of the intrusion (~21.3 wt.%) and broadly increase outward toward the intrusion margins (21.8 wt.% at the base; 22.2 wt.% at the top), with Cr_2O_3 following the same pattern (0.5 to 0.1 wt.%) as the olivine Fo.

Mineral compositions in UZA are highly variable, covering the full range observed in the MZ and LZ, with no clear stratigraphic trends (Fig. 13). The most pronounced stratigraphic variations in UZA occur in the highly poikilitic orthocumulates, in which clinopyroxene has consistently low Cr_2O_3 contents (<0.05 wt.%). Sample 22CCCI5-09 (351.8 m) contains notably forsteritic olivine (mean Fo_{75}). Although there were no olivine grains suitable for analysis in sample 22CCCI5-12 (315.9 m), it contains plagioclase with a wide range of core compositions ($An_{61.0}$ to $An_{88.1}$: Fig. 13).

The olivines at the base and top of UZB have elevated Fo contents (mean Fo_{71} and Fo_{69}), becoming less forsteritic as olivine decreases in abundance in the upper–central parts of the UZB stratigraphy (Fo_{64}; c.f. Fig. 4). Plagioclase becomes more anorthitic upward (An_{80} to An_{85}; Fig. 13). Olivine in sample 22CCCI3-33 (494.0 m), collected from an anomalously olivine-rich horizon, is relatively forsteritic (Fo_{67}), and is associated with plagioclase cores spanning a wide compositional range (An_{67} to An_{86}; Fig. 13).

Links between bulk-rock compositions and microstructures

The relative proportions of olivine, clinopyroxene, and plagioclase exert a primary control on the bulk-rock geochemistry, with the cumulus/intercumulus nature of clinopyroxene evident in variations of bulk-rock Al_2O_3 and CaO with MgO (Fig. 14; Supplementary Fig. S1). This is linked to the bimodal variation of Θ_{cpp}, which varies with the liquidus assemblage of the bulk magma (Holness *et al.*, 2007b; 2013): low values are associated with a bulk magma saturated in only olivine and plagioclase, and high values with a magma saturated additionally in clinopyroxene.

The combination of bulk-rock variation (Fig. 14) and bimodality of Θ_{cpp} (Fig. 5) provides a reliable means to distinguish the LZ from the overlying units: the LZ cumulus assemblage, of olivine and minor plagioclase, results in a compositional trend extending towards the average olivine compositions analysed in the gabbros, and low values of Θ_{cpp}. By contrast, the MZ and UZB (and, to a lesser extent, UZA) bulk-rock compositions display compositional trends between the clinopyroxene and plagioclase nodes: this, together with the high values of Θ_{cpp}, demonstrate that clinopyroxene formed as a cumulus phase. Those samples of UZB that are closest to the plagioclase mean composition are those with poikilitic clinopyroxene.

DISCUSSION

Emplacement setting and intrusion geometry

Interpreting the evolution of the Carlingford Later Gabbros first requires a consideration of their emplacement setting and intrusion geometry. The shape of an igneous intrusion, and its relationship with the surrounding country rock, exerts a fundamental control on its thermal evolution. In turn, the thermal evolution dictates the dynamics of magma system development, influencing the degree of quenching, crystal growth morphology, the vigour of convection, and magma rheology. The orientation and symmetry of thermal gradients can also control compositional profiles across layered mafic systems (e.g., Lesher & Walker, 1988, McBirney, 1985).

The pillowed and net-veined dolerites observed at Cooley Castle Quarry (Fig. 3e), and the chilling of dolerite in contact with recrystallised microgranite margins (Fig. 3f), are interpreted to result from granitic back-veining, in agreement with Bailey (1961) and indicating the older age of the microgranite. We suggest the diffuse microgranite-gabbro contact preserved at the base of the drill core at Slieve Foye core is a consequence of partial melting of an older microgranite followed by hybridisation with the intruding gabbro: this contact perhaps represents the true base of the layered gabbros at this locality. These observations thus support the suggestion (O'Driscoll, 2006; Meade *et al.*, 2014) that the gabbros intruded an earlier, relatively warm, shallow body of silicic magma. The resulting thermal buffering would have maintained high temperatures within the gabbroic bodies (Annen, 2017), permitting not only various differentiation processes that resulted in the mineralogical and geochemical trends described earlier, but also the strong bimodality of Θ_{cpp} which requires internal thermal buffering through much of the crystallisation history of the Later Gabbros (Holness *et al.,* 2013).

Although Le Bas (1960; 1970) recognised the inward-dipping layers of the Carlingford gabbros, the floor of the intrusion was approximated as sub-horizontal, capping the mountains that form a ring around the complex (Fig. 2a). Though we suspect that the base of the chamber is not generally planar, our structural data (Fig. 1c; Supplementary Table 5), in conjunction

with anisotropy of magnetic susceptibility measurements (O'Driscoll, 2006), imply that the layered gabbros dip beneath the microgranites exposed in the centre of the complex, in agreement with the models developed by Buchanan (1985), Meade (2008) and Meade *et al.* (2014) (Fig. 2b). We therefore propose that, during emplacement, much of the gabbro was thermally insulated by granitic material both above and below (Fig. 15).

Note that Le Bas (1965) mapped a body of Later Gabbros at Spellickanee, interpreted as a ring separating vent agglomerates from the surrounding microgranites (Fig. 1b). The poor exposure in this region (a feature which was also mentioned in early surveys; Traill, 1878) precludes a definitive answer, but we reinterpret the gabbro outcrops here as isolated blocks within the agglomerate (Fig. 15), consistent with Richey's (1932) description of these rocks as "shattered eucrites".

Revised stratigraphy of the Later Gabbros

Our revised stratigraphy of the Carlingford Later Gabbros builds upon the subdivisions proposed by Le Bas (1960)**,** with the downwards extension from drill core material permitting the identification of our LZ. The "poikilitically-enclosed olivine-rich rocks" described by Le Bas (1960) likely refers to the localised exposures of the top of LZ, though it was considered a marginal feature. Our work has revealed several compositional trends that do not conform with Le Bas's original subdivisions, which were created using a large number of scattered samples distributed over a wide area, in contrast to our linear transects through the stratigraphy. Units E1 and E2 have been combined to form the MZ, with petrographic and geochemical trends showing continuous trends that cross the unit boundaries. While UZA loosely corresponds with E3, there are no coherent trends in our data, inconsistent with Le Bas's observations. UZB, however, follows the general mineralogical and geochemical trends described for E4 (Table 1).

Emplacement model

Lower Zone: Pulsed inflation of a liquid-rich chamber

The geochemical and microstructural trends in the LZ reveal broadly slash-shaped profiles (per Egorova & Latypov, 2013), with each cyclic subunit showing a basal enrichment in idiomorphic, often clustered, olivine, which grade upwards to compositions richer in plagioclase, which coarsens upwards. We suggest that the series of cyclic units that comprise the LZ record pulsed inflation of a crystal-poor magma chamber by magma saturated primarily in olivine and plagioclase, followed by crystal settling on the floor.

Stokes' settling velocities (Richardson & Zaki, 1954) were calculated using measured mineral grain diameters, together with a liquid composition taken from the most aphyric mafic cone sheet reported from Carlingford (Meade *et al.*, 2014). Calculations assume spherical grains in a liquid-dominated environment. These calculations provide first-order constrains for the efficiency of mineral settling in a liquid-dominated environment, though processes such as hindered settling may decreases these timescales (Faroughi & Huber, 2015; Huber *et al*., 2025b). The calculated maximum velocities (Fig. 16) show that olivine and clinopyroxene settle regardless of grain size, whilst plagioclase transitions from neutrally buoyant to buoyant as grain size increases.

Our microstructural observations are consistent with the olivine-rich bases of each cyclic subunit forming by settling of olivine grains which either grew post-emplacement or formed a cargo in the replenishing magma. The upwards-reduction in olivine abundance, together with an average bulk-rock MgO content of 11.2 wt. %, that is, somewhat higher than values of ~10 wt. % expected for parental basaltic magmas (Elthon, 1979), is supportive of some olivine accumulation. The olivine clusters formed by synneusis prior to settling (cf. Shiant Isles; Holness *et al*., 2017). While some plagioclase grains likely formed clusters with the olivine, permitting settling to form a loosely-packed olivine-plagioclase framework in which clinopyroxene crystallised interstitially, the coarsening-upwards of the plagioclase is

suggestive of continued growth of buoyant grains which settled only if clustered with denser phases (Holness *et al.*, 2017). Continued solidification of the interstitial liquid resulted in overgrowths of primocrysts and irregular grain boundaries.

A general upwards increase through the LZ of plagioclase anorthite contents, plagioclase abundance, bulk-rock Sr contents and, to a lesser extent, increasingly primitive olivine compositions, suggests that the replenishing magmas became progressively more mafic. A possible mechanism for this is the gradual emptying of a deeper magma reservoir that was compositionally stratified.

Further refinement of this model is possible with a close examination of the cyclic units, which can be broadly divided into three groups (Fig. 11). Units C1-C6 are characterised by comparatively weakly defined olivine-rich bases (Fig. 6), shown by relatively low MgO and Ni contents, but high Cr_2O_3 (Fig. 11), reflecting elevated Cr concentrations in the clinopyroxenes (Fig. 13b). These basal units have high dihedral angles (~97°; Fig. 5a) indicative of a bulk magma saturated in olivine, plagioclase, and clinopyroxene, demonstrating that clinopyroxene was a liquidus phase despite its apparently intercumulus habit (Fig. 4b). This suggests that clinopyroxene formed part of the crystal population settling to the floor, with the anhedral habit indicative of substantial interstitial overgrowth. In contrast, units C7-C9 display more pronounced olivine-rich bases (Fig. 6) and lower values of Θ_{cpp} (~87°; Fig 5b), indicative of two-phase cotectic crystallisation of only olivine and plagioclase. Units C10 and C11 do not have a well-defined slash-shaped profile (Fig. 11), and may be the product of a more complex, multi-stage replenishment history, or smaller scale cumulate intervals that are not discernible with our sample spacing.

The clinopyroxene mode tends to decrease upwards through the cyclic units, irrespective of whether clinopyroxene was a liquidus phase (Fig. 4). We suggest that in units where clinopyroxene was not a liquidus phase (i.e. low Θ_{cpp}), accumulation of olivine and high-aspect

ratio plagioclase grains created a high porosity mush that permitted extensive intercumulus pyroxene growth. For those units in which clinopyroxene was a primocryst phase (high Θ_{cpp}), the high porosity of the mush at the base also permitted extensive overgrowth of the pyroxene primocrysts.

Extensive overgrowth of clinopyroxene from abundant interstitial liquid is recorded by the strong compositional zoning and presence of oxide inclusions towards the rims (Fig. 12). An inverse relationship between plagioclase An and clinopyroxene CaO through the LZ (Fig. 13) demonstrates the interplay between the cumulus and intercumulus phases, with the partitioning of Ca between clinopyroxene and plagioclase controlled by the extent of prior plagioclase crystallisation. The positive correlation between olivine Fo content and the concentration of Cr_2O_3 in the associated clinopyroxene is likely to be a consequence of simultaneous crystallisation.

The bimodal dihedral angle population in the LZ and its association with the liquidus assemblage implies that there was only limited late-stage melt migration of the sort observed in the Rum Eastern Layered Series, resulting in low dihedral angles therein (cf. Holness, 2007, Holness *et al.*, 2012, Leuthold *et al.*, 2014). This, together with the well-defined geochemical and microstructural transitions separating the cyclic units, is consistent with a thin mush zone.

High median values of Θ_{cpp} are observed in the two lowermost samples of the Southeast Foye transect, indicative of the bulk magma being saturated in clinopyroxene. This appears inconsistent with the evidence for substantial interstitial growth and is in contrast with the low dihedral angles observed at this stratigraphic height in the drill core and at North Foye. Despite being only ~525 m along-strike from the drill core (Fig. 1c), this is suggestive of lateral differences in the bulk liquid, due perhaps to inefficient mixing and limited lateral convective flow.

Together, the LZ records pulsed inflation of a liquid-rich magma chamber, with efficient settling of cumulus crystal aggregates to form thin mush layers with subsequent *in situ* crystallisation at the base. The resulting cyclic units closely resemble cyclic stratigraphy described from the Rum Eastern Layered Intrusion, Megacyclic Unit II of Sept Iles, and the Upper Main Zone and Upper Zone of the western Bushveld Complex (Namur *et al*., 2010; Tegner *et al*., 2006; Emeleus & Troll, 2014). At Rum, macro-rhythmic units are attributed to periodic magma replenishment followed by crystal settling (Renner & Palacz, 1987; Emeleus *et al.*, 1996), with the overall thickness affected by eruption (Holness & Winpenny, 2008), although recent work has suggested some *in situ* crystallisation and reactive melt migration (Leuthold *et al.*, 2014; Hepworth *et al.*, 2017). Similarly, plagioclase-rich cyclic cumulates at Sept Iles record repeated replenishment, where *in situ* crystallisation and the development of polycrystalline chains are inferred to have inhibited plagioclase flotation (Namur *et al.*, 2010; 2015). Basal reversals, characteristic of both Sept Iles and Bushveld cyclic units, are widely attributed to vigorous convection and mixing between successive batches (Kruger & Smart, 1987; Tegner *et al.*, 2006; Namur *et al.*, 2010; 2015). Their absence in the LZ at Carlingford likely reflects the smaller volume of individual replenishment events (i.e. an order of magnitude thinner than those in these global analogues) resulting in less efficient mixing.

Middle Zone: Fractionation and crystal settling in a liquid-rich chamber

A shift to high Θ_{cpp} and the appearance of abundant, compact clinopyroxene at the base of the MZ signal the saturation of the bulk magma in clinopyroxene. The associated change to more evolved compositions of plagioclase and olivine record the introduction of a compositionally distinct magma. The continuous geochemical and microstructural trends through the MZ stratigraphy, laterally continuous across the two outcrop transects over > 1.7 km (Fig. 1c), indicate a large and well-mixed body of magma that remained essentially closed during its development. The presence of a deep, convecting body of crystal-poor liquid is consistent with the development of cm-scale layering (Fig. 3c). Similarly, the trough-shaped rhythmic layering

(Fig. 3c; O'Driscoll, 2006) is suggestive of convective transport and deposition of dense crystal slurries on the chamber floor. We therefore argue that the base of the MZ marks the essentially instantaneous arrival of a large batch of magma, representing rapid inflation of the system, and the transition from small batch replenishment to a large liquid-dominated, well-mixed, system that underwent progressive fractionation by the settling of crystals to the floor. The absence of a compositional reversal, or evidence of quenching, at the top of the MZ, suggests that the roof of the liquid-rich body that formed the MZ is not preserved, perhaps due to thermal erosion (Huppert & Sparks, 1989).

The Fo- and Cr_2O_3-rich olivine and clinopyroxene at the base of the MZ records the settling of the earliest-formed most primitive crystals from the new magma influx. An early phase of dendritic pyroxene growth is indicative of quenching of this incoming magma at the floor of the magma body. Plagioclase grains at the base often occur as well-sintered aggregates with 120° triple junction grain boundaries (Supplementary Fig. S3) and display a wide compositional variability, suggestive of a mixed population that may have been introduced as crystal cargo.

The reduction in Fo content of olivine and Cr_2O_3 content of clinopyroxene upwards through the MZ, and a gradation towards more plagioclase-rich mesocumulates and orthocumulates, is associated with an increase in the anorthite content of the plagioclase. This apparent paradox can be resolved by considering the relative density of the three primocryst phases. Buoyant plagioclase accumulates towards the top of the liquid-rich MZ magma body, with the upwards increase of grain size and reduction of aspect ratio due to the positive feedback of increasing buoyancy as the grains undergo prolonged periods of growth while suspended in the convecting magma (Fig. 16).

These observations indicate that the MZ records the rapid establishment of a large liquid-rich magma reservoir within which differentiation was controlled by crystal settling, flotation and

convection. Systematic, intrusion-scale modal, geochemical and microstructural trends, together with the presence of pseudosedimentary structures, closely resemble those documented in the Skaergaard Intusion (Thy *et al.*, 2023) and the picrodolerite-crinanite unit of the Shiant Isles Main Sill (Gibb & Henderson, 2006; Holness *et al.*, 2017). In Carlingford, these features mark a fundamental shift from incremental replenishment to sustained melt emplacement.

Notably, the MZ lacks clear marginal reversals that define S-shaped compositional profiles reported from several mafic intrusions (Egorova & Latypov, 2013; Latypov, 2015) and modern lava lakes (e.g. Kilauea Iki: Helz, 1980; Marsh, 1996). Such profiles are commonly attributed to decreasing solidification rates during chamber inflation (Marsh, 1996) or *in situ* crystallisation of progressively more mafic magma prior to large-scale crystal settling (Egorova & Latypov, 2013; Latypov, 2015; Gibb & Henderson, 2006). Their absence in Carlingford suggests that inflation occurred as a single event, with mechanical differentiation operating within a thermally buffered system that was potentially stabilised by the insulating effect of the slightly older microgranites and/or gabbros.

Upper Zone A: Chaotic sill emplacement

The UZA gabbros encompass a wide range of compositions and microstructures, with no systematic stratigraphic trends and no lateral continuity between our two transects. In contrast to the LZ and MZ, in which the compositions of olivine and clinopyroxene are correlated, the decoupling of olivine Fo content and clinopyroxene Cr_2O_3 concentration in UZA implies that these minerals are not following the same fractionation trends, perhaps reflecting a more complex, open system incorporating antecrysts. While clinopyroxene at North Foye is consistently a cumulus phase, crystal habit and Θ_{cpp} suggest that it oscillates on and off the liquidus at Southeast Foye. Additionally, there are significant lateral bulk-rock geochemical variations, suggesting that the UZA magmas were inefficiently mixed and laterally

discontinuous. This evidence, together with observations of small, layer-parallel, intrusive bodies (Fig. 3d), indicates that UZA represents the chaotic emplacement of multiple, laterally discontinuous sills in a crystal-rich environment.

Local evidence for lateral magma flow is preserved in UZA: sample 22CCCI3-21 (Fig. 9b) is a quenched plagioclase-rich gabbro with a strong foliation formed by high aspect ratio plagioclase laths, consistent with flow alignment in a crystal slurry. Similarly, the base of UZA is marked by a fine-grained adcumulate gabbro which may have formed by crystal accumulation from density currents, though whether the liquid-rich nature of this part of UZA was the remnants of an earlier extensive magma body preserved as MZ, or a laterally injected sill, remains uncertain.

Our data indicate that the UZA records repeated magma injection into a mechanically coherent, crystal-rich mush, producing chaotic stratigraphic trends consistent with models of non-sequential amalgamated sill intrusion (Mungall *et al.*, 2016; Wall *et al.*, 2018; Latypov *et al.*, 2024). The Rum Western Layered Intrusion, where macro-rhythmic layering is poorly developed relative to the Eastern Layered series (Hepworth *et al.*, 2018), provides a close analogue, with out-of-sequence melt injection and internal mush reworking generating intrusion-scale heterogeneity expressed as irregular gabbroic layers, lenses, and apophyses (Hepworth *et al.*, 2018). At Carlingford, planar gabbroic contacts with limited exchange imply sill emplacement into largely sub-solidus pre-existing units, nevertheless supporting a similarly chaotic, sill-dominated mode of construction.

Upper Zone B: Combined liquid–solid intrusion and melt infiltration

Building on our interpretations of the MZ, the geochemical and modal stratification preserved in UZB, with an upwards-increase in plagioclase An content and modal abundance, and the basal olivine-clinopyroxene adcumulate, is interpreted as the record of increasing flotation of plagioclase leading to accumulation at the top of a liquid-rich magma body, while denser mafic

phases settled to the floor. Thus, UZB records the fractionation and solidification of a large liquid-rich body comparable to that which formed the MZ. However, the broad stratigraphic trends are locally disrupted by small-scale sill-like intrusions, and potentially modification by late-stage fluid infiltration.

In detail, the anomalously olivine-rich horizon at 494.0 m is interpreted to represent a small sill-like intrusion analogous to those of UZA. Towards the top of the unit, the reappearance of olivine within plagioclase-rich cumulates likely reflects the flotation of olivine entrained with buoyant clusters of plagioclase. The wide range of olivine composition and morphology suggests that several different grain populations were reworked in a convecting intrusion.

Whilst clinopyroxene abundances broadly follow expected stratigraphic trends (Fig. 4a), there is no correlation with their composition (Fig. 13b, 13c). For example, the most Cr-rich (and therefore most primitive) clinopyroxene cores are found towards the centre of UZB, rather than at its base. Importantly, a shift from a cumulus to interstitial clinopyroxene occurs at ~504.9 m, which is preceded by a compositional gap in bulk-rock Al_2O_3 and MgO contents (Fig. 14) and a graded transition from high to low Θ_{cpp} (Fig. 5a). This may be the result of late-stage modification by the infiltration of reactive melt in a similar manner to that inferred for the Rum Eastern Layered Intrusion (Holness, 2007; Holness *et al.*, 2012; Leuthold *et al.*, 2014).

The combination of higher olivine Fo values, a greater division between cumulates formed by flotation and those formed by settling, and the pronounced geochemical variability through the UZB stratigraphy, suggest that UZB represents the solidification of a convecting open system replenished by multiple bodies of magma.

Temporal evolution and crustal structure of the Later Gabbros

The internally coherent cyclic packages comprising the LZ, interpreted here as gravitational accumulations of primocrysts from a succession of liquid-rich magma bodies, are consistent with sequential emplacement of individual batches younging upwards, broadly analogous to

the cyclic units of the Rum Eastern Layered Series (Renner & Palacz, 1987; Emeleus *et al.*, 1996; Holness & Winpenny, 2008). Cooling rates calculated for upper-crustal magma bodies indicate that replenishment in the LZ may have occurred on timescales of the order years to decades (Irvine, 1970; Cawthorn, 2012). The dendrite-like pyroxene morphology at the base of the MZ is suggestive of supersaturation consequent to quenching, with the corollary that the MZ postdated the LZ and was likely emplaced rapidly as a single large magma body, consistent with its laterally continuous, systematic stratigraphic trends.

Conversely, the timing of the Upper Zones is more ambiguous. The chaotic internal structure of UZA, including laterally discontinuous sills, precludes the determination of any relative timing of emplacement. UZB, although more stratigraphically ordered, also contains sill-like intrusions, implying that its emplacement may have overlapped with the construction of UZA. Though the relative order of intrusion of these units remains unresolved, the temporal evolution of the Later Gabbros is unlikely to be clarified through isotopic dating, with reported ages for the gabbros carrying uncertainties exceeding timescales proposed for other Paleogene intrusions (Wotzlaw *et al.*, 2012; Emeleus & Troll, 2014).

Despite these chronological uncertainties, our data suggest that the Carlingford Later Gabbros evolved neither exclusively as a persistent, melt-rich magma chamber nor as a purely incremental crystal mush system. Rather, the intrusion records a continuum of emplacement styles, sometimes overlapping over short spatial and temporal scales (Fig. 17). These transitions are consistent with variations in melt flux, which control the thermal state of the system (Annen, 2017; Sparks *et al.*, 2019; Humphreys *et al.*, 2025): sustained high magma flux maintains melt-rich conditions and promotes chamber-like behaviour (e.g. the MZ), whereas sporadic input favours disordered, mush-dominated sill assembly (e.g. in UZA). Within this framework, the LZ records rapid pulsed intrusion, while UZB reflects waning flux and increasing crystallinity during progressive cooling of an initially molten intrusion (Huber *et al.*, 2009). This effect may be exacerbated by the progressive cooling of the surrounding

microgranites, reducing thermal insulation and promoting more mushy conditions for later replenishments (Annen, 2017).

The significance of these findings extends to competing deposit models for platinum-group elements (PGE) mineralisation (Mungall & Naldrett, 2008). Replenishment within liquid-rich environments, like that described for the LZ and MZ, is conducive to classical models of reef-style sulphide mineralisation. In these models, exsolved sulphide liquids can efficiently scavenge chalcophile PGE in a convective melt, then settling to form thin, high-tenor horizons at the base of the intrusion (Campbell & Naldrett, 1979; Holwell & McDonald, 2010; Zientek, 2012). Alternatively, metasomatic models involving PGE collection and concentration via the ascent of percolative reactive fluids through crystal mushes are more consistent with our Upper Zones (Barnes & Campbell, 1988; Boudreau & McCallum, 1992; Boudreau & Meurer, 1999).

This dynamic assembly has direct implications for volcanic behaviour in plume-related settings. The cyclic replenishment of progressively more mafic magma in the LZ, for example, may reflect episodic replenishment events coupled with discrete pulses of volcanic activity (e.g. Holness & Winpenny, 2008; Giuffrida *et al.*, 2025), whereas the MZ marks a period of high melt flux capable of driving more voluminous eruptions (Cawthorn, 2012; Annen *et al.*, 2022). Buoyancy-driven plagioclase accumulation, observed towards the roof of the MZ and UZA, corresponds to features observed in erupted products and has been proposed as a key mechanism in facilitating the entrainment of crystals in plagioclase-rich ocean island basalts, thereby modulating eruptive style on annual-to-millennial timescales.

Cone sheet geometries (Halsall, 1974; Schauroth *et al.*, 2014), geophysical surveys (Cook & Murphy, 1952; Hodgson & Young, 2016; Sajjadi *et al.*, 2020), and inherited crystal cargo imply the existence of a deeper reservoir (Fig. 15), placing the layered gabbros as a shallow melt-rich storage region of a more vertically extensive crustal system (e.g. Edmonds *et al.*, 2019), possibly linked to the Slieve Gullion Complex (Meade *et al.*, 2014). However, available data

lack the resolution required to constrain its internal structure. Compositional shifts between high- and low-Fo olivines, both within and between units, may reflect either prolonged hiatuses between injections from an evolving, single deeper reservoir or contemporaneous input from multiple, compositionally distinct, magma sources. Further work on the Carlingford Complex should be aimed at constraining the nature of the underlying, deeper, reservoir. Fragments of mush entrained in the associated cone sheets (Fig. 3a) may provide key geochemical and barometric information on the interconnectivity of the deeper reservoir, including potential links to the adjacent Slieve Gullion Complex (Fig. 1a). Likewise, closer investigation of magma mixing and assimilation interactions could help assess their role in controlling magma rheology and eruptibility.

CONCLUSIONS

Integrated geochemical and microstructural analyses of the Carlingford Later Gabbros reveal four discrete stratigraphic zones, preserving evidence of liquid- and crystal-rich modes of magma replenishment. Our findings demonstrate that subvolcanic systems can shift between contrasting emplacement regimes over relatively short spatial and temporal intervals.

The LZ records episodic replenishment and cumulate development in an open, liquid-dominated environment, whereas the MZ represents high melt flux into a near-closed system, facilitating large-scale crystal settling, flotation and convection. UZA represents sporadic intrusion of compositionally variable, laterally discontinuous sills in a crystal-rich environment. The record of UZB is primarily of the inflation of a convective, liquid-rich body superimposed on which is evidence of infiltration of late-stage liquids into existing mush zones, and the intrusion of later sills.

The Carlingford Later Gabbros demonstrate that layered intrusions need not conform to a strict ‘magma chamber’ versus ‘mush’ dichotomy. Instead, their construction can transition between these behavioural endmembers as a result of changes in melt flux and thermal state. This

dynamic assembly has implications for ore mineralisation in layered intrusions, on which the models are based. Given that the Carlingford Complex preserves the shallow-crustal architecture of a once-active volcanic centre, we suggest the development of the layered gabbros would likely have mirrored eruptive processes at the surface.

ACKNOWLEDGEMENTS

This publication has emanated from research conducted with the financial support of Research Ireland and Geological Survey Ireland under grant number 20/FFP-P/8895. Bulk-rock geochemical analysis was supported by the Geological Survey Ireland-funded Earth Surface Research Laboratory in Trinity College Dublin. Paul Guyett is thanked for assistance with SEM data collection. We are grateful to Pat O'Sullivan and those at the Geological Survey Ireland Core Store for access to drill core material. Maura Morgan, Sarah Carty, and Francis Hedron are thanked for their assistance with sample preparation.

REFERENCES

Annen, C. (2017). Factors affecting the thickness of thermal aureoles. *Frontiers in Earth Science* **5**, 82. https://doi.org/10.3389/feart.2017.00082

Annen, C., Latypov, R., Chistyakova, S., Cruden, A. R. & Nielsen, T. F. (2022). Catastrophic growth of totally molten magma chambers in months to years. *Science Advances* **8**, eabq0394. doi: 10.1126/sciadv.abq0394. https://doi.org/10.1126/sciadv.abq0394

Bachmann, O. & Bergantz, G. W. (2004). On the origin of crystal-poor rhyolites: extracted from batholithic crystal mushes. *Journal of Petrology* **45**, 1565-1582. https://doi.org/10.1093/petrology/egh019

Bagnold, R. A. (1954). Experiments on a gravity-free dispersion of large solid spheres in a Newtonian fluid under shear. *Proceedings of the Royal Society of London. Series A. Mathematical and Physical Sciences* **225**, 49-63. https://doi.org/10.1098/rspa.1954.0186

Bailey, E. B. (1961). Mobilisation of granophyre in Eire and sinking of olivine in Greenland. *Geological Journal* **2**, 143-154. https://doi.org/10.1002/gj.3350020202

Barnes, S. J. & Campbell, I. H. (1988). Role of late magmatic fluids in Merensky-type platinum deposits: a discussion. *Geology* **16**, 488-491. https://doi.org/10.1130/0091-7613(1988)016%3C0488:ROLMFI%3E2.3.CO;2

Boudreau, A. & McCallum, I. (1992). Concentration of platinum-group elements by magmatic fluids in layered intrusions. *Economic Geology* **87**, 1830-1848. https://doi.org/10.2113/gsecongeo.87.7.1830

Boudreau, A. & Meurer, W. (1999). Chromatographic separation of the platinum-group elements, gold, base metals and sulfur during degassing of a compacting and solidifying igneous crystal pile. *Contributions to Mineralogy and Petrology* **134**, 174-185. https://doi.org/10.1007/s004100050477

Buchanan, D. L. (1985). The Economic Potential of the Layered Mafic Rocks of the Carlingford Complex, Ireland.: Westland Exploration Limited.

Buchanan, D. L. (2012). *Platinum-group element exploration*: Elsevier.

Campbell, I. & Naldrett, A. (1979). The influence of silicate: sulfide ratios on the geochemistry of magmatic sulfides. *Economic Geology* **74**, 1503-1506. https://doi.org/10.2113/gsecongeo.74.6.1503

Carter, E. J., Stock, M. J., Beresford-Browne, A., Cooper, M. R., Raine, R. & Fereyrolles, A. (2024). Volcanic tempo driven by rapid fluctuations in mantle temperature during large igneous province emplacement. *Earth and Planetary Science Letters* **644**, 118903. https://doi.org/10.1016/j.epsl.2024.118903

Cashman, K. V., Sparks, R. S. J. & Blundy, J. D. (2017). Vertically extensive and unstable magmatic systems: a unified view of igneous processes. *Science* **355**, eaag3055. https://doi.org/10.1126/science.aag3055

Cawthorn, R. G. (2012). Multiple sills or a layered intrusion? Time to decide. *South African Journal of Geology* **115**, 283-290. https://doi.org/10.2113/gssajg.115.3.283

Charlesworth, J. K. (1960). The Geology of north-east Ireland. *Proceedings of the Geologist's Assocation of London* **71**, 429.

Cook, A. H. & Murphy, T. (1952). *Measurements of gravity in Ireland. Gravity survey of Ireland*: Dublin Institute for Advanced Studies.

Cooper, K. M. (2019). Time scales and temperatures of crystal storage in magma reservoirs: implications for magma reservoir dynamics. *Philosophical Transactions of the Royal Society A: Mathematical, Physical and Engineering Sciences* **377**. https://doi.org/10.1098/rsta.2018.0009

Cooper, M. (2004). Mantle plumes, ocean spreading and the North Atlantic Igneous Province, Palaeogene extrusive igneous rocks, Northern Ireland. *The Geology of Northern Ireland-Our Natural Foundation*. Belfast, Northern Ireland: Geological Survey of Northern Ireland.

Cooper, M., Johnston, T. & Mitchell, W. (2004). Palaeogene intrusive igneous rocks. *The Geology of Northern Ireland: Our Natural Foundation*, 179-198.

Cooper, M., Tapster, S. & Condon, D. (2020). Feeling the pulse? New high resolution U-Pb zircon geochronological constraints for the Northern Ireland sector of the North Atlantic Igneous Province. *EGU General Assembly Conference Abstracts*, 8464. https://doi.org/10.5194/egusphere-egu2020-8464

De, S. & Poole, A. B. (1974). The Relationship between the Acid and Basic Rocks near Carlingford, Co. Louth. *Proceedings of the Royal Irish Academy. Section B: Biological, Geological, and Chemical Science*, 381-402.

Edmonds, M., Cashman, K. V., Holness, M. & Jackson, M. (2019). Architecture and dynamics of magma reservoirs. The Royal Society Publishing, 20180298. https://doi.org/10.1098/rsta.2018.0298

Egorova, V. & Latypov, R. (2013). Mafic–ultramafic sills: New insights from M-and S-shaped mineral and whole-rock compositional profiles. *Journal of Petrology* **54**, 2155-2191. https://doi.org/10.1093/petrology/egt045

Elthon, D. (1979). High magnesia liquids as the parental magma for ocean floor basalts. *Nature* **278**, 514-518. https://doi.org/10.1038/278514a0

Emeleus, C. H. & Bell, B. R. (2005). *British Regional Geology: the Palaeogene volcanic districts of Scotland* Nottingham: British Geological Survey

Emeleus, C. H., Cheadle, M. J., Hunter, R. H., Upton, B. G. J. & Wadsworth, W. J. (1996). The Rum layered suite. *Developments in petrology*: Elsevier, 403-439. https://doi.org/10.1016/S0167-2894(96)80014-5

Emeleus, C. H. & Troll, V. R. (2014). The rum igneous centre, Scotland. *Mineralogical Magazine* **78**, 805-839. https://doi.org/10.1180/minmag.2014.078.4.04

Evans, A. L., Fitch, F. J. & Miller, J. A. (1973). Potassium-argon age determinations on some British Tertiary igneous rocks. *Journal of the Geological Society* **129**, 419-438. https://doi.org/10.1144/gsjgs.129.4.0419

Faroughi, S. A. & Huber, C. (2015). Unifying the relative hindered velocity in suspensions and emulsions of nondeformable particles. *Geophysical Research Letters* **42**, 53-59. https://doi.org/10.1002/2014GL062570

Gibb, F. & Henderson, C. (2006). Chemistry of the Shiant Isles Main Sill, NW Scotland, and wider implications for the petrogenesis of mafic sills. *Journal of Petrology* **47**, 191-230. https://doi.org/10.1093/petrology/egi072

Giordano, D., Russell, J. K. & Dingwell, D. B. (2008). Viscosity of magmatic liquids: a model. *Earth and Planetary Science Letters* **271**, 123-134. https://doi.org/10.1016/j.epsl.2008.03.038

Giuffrida, M., Salerno, G. & Viccaro, M. (2025). Multiple magma recharges over prolonged period ultimately trigger eruptions at Vulcano, Aeolian Islands. *Scientific Reports* **15**, 1260. https://doi.org/10.1038/s41598-025-85496-z

González-Guzmán, R., Elizondo-Pacheco, L. A., González-Roque, A., Sánchez-Torres, C. E. & Cárdenas-Muñoz, K. S. (2023). shinyNORRRM: A cross-platform software to calculate the CIPW norm. *Mathematical Geosciences* **55**, 563-577. https://doi.org/10.1007/s11004-023-10052-2

Griffith, R. (1840). Presidential Address. *Journal of the Geological Society of Dublin*, 95-130.

Halsall, T. J. (1974). The minor intrusions and structure of the Carlingford complex, Eire. University of Leicester.

Helz, R. T. (1980). Crystallization history of Kilauea Iki lava lake as seen in drill core recovered in 1967–1979. *Bulletin Volcanologique* **43**, 675-701. https://doi.org/10.1007/BF02600365

Hepworth, L. N., O'Driscoll, B., Gertisser, R., Daly, J. S. & Emeleus, C. H. (2017). Incremental construction of the unit 10 Peridotite, Rum eastern layered intrusion, NW Scotland. *Journal of Petrology* **58**, 137-166. https://doi.org/10.1093/petrology/egx008

Hepworth, L. N., O'Driscoll, B., Gertisser, R., Daly, J. S. & Emeleus, C. H. (2018). Linking in situ crystallization and magma replenishment via sill intrusion in the Rum Western Layered Intrusion, NW Scotland. *Journal of Petrology* **59**, 1605-1642. https://doi.org/10.1093/petrology/egy073

Higgins, O., Stock, M. J., Geist, D., Neave, D. A., Buisman, I., Bernard, B. & Gleeson, M. (2025). Annual-to-millennial fluctuations in the physical properties of crystal-rich magma storage zones. *Communications Earth & Environment*. https://doi.org/10.1038/s43247-025-02982-y

Hildreth, W. (2004). Volcanological perspectives on Long Valley, Mammoth Mountain, and Mono Craters: several contiguous but discrete systems. *Journal of Volcanology and Geothermal Research* **136**, 169-198. https://doi.org/10.1016/j.jvolgeores.2004.05.019

Hodgson, J. & Young, M. (2016). The Tellus airborne geophysical surveys and results. Royal Irish Academy.

Holness, M. (2007). Textural immaturity of cumulates as an indicator of magma chamber processes: infiltration and crystal accumulation in the Rum Eastern Layered Intrusion. *Journal of the Geological Society* **164**, 529-539. https://doi.org/10.1144/0016-76492006-021

Holness, M. B., Farr, R. & Neufeld, J. A. (2017). Crystal settling and convection in the Shiant Isles Main Sill. *Contributions to Mineralogy and Petrology* **172**, 7. https://doi.org/10.1007/s00410-016-1325-x

Holness, M. B., Hallworth, M. A., Woods, A. & Sides, R. E. (2007a). Infiltration metasomatism of cumulates by intrusive magma replenishment: the Wavy Horizon, Isle of Rum, Scotland. *Journal of Petrology* **48**, 563-587. https://doi.org/10.1093/petrology/egl072

Holness, M. B., Humphreys, M. C. S., Sides, R., Helz, R. T. & Tegner, C. (2012). Toward an understanding of disequilibrium dihedral angles in mafic rocks. *Journal of Geophysical Research: Solid Earth* **117**. https://doi.org/10.1029/2011JB008902

Holness, M. B., Namur, O. & Cawthorn, R. G. (2013). Disequilibrium dihedral angles in layered intrusions: a microstructural record of fractionation. *Journal of Petrology* **54**, 2067-2093. https://doi.org/10.1093/petrology/egt041

Holness, M. B., Nielsen, T. F. D. & Tegner, C. (2007b). Textural maturity of cumulates: a record of chamber filling, liquidus assemblage, cooling rate and large-scale convection in mafic layered intrusions. *Journal of Petrology* **48**, 141-157. https://doi.org/10.1093/petrology/egl057

Holness, M. B., Stock, M. J. & Geist, D. (2019). Magma chambers versus mush zones: constraining the architecture of sub-volcanic plumbing systems from microstructural analysis of crystalline enclaves. *Philosophical Transactions of the Royal Society A* **377**, 20180006. https://doi.org/10.1098/rsta.2018.0006

Holness, M. B. & Winpenny, B. (2008). The Unit 12 allivalite, Eastern Layered Intrusion, Isle of Rum: a textural and geochemical study of an open-system magma chamber. *Geological Magazine* **146**, 437-450. https://doi.org/10.1017/S0016756808005797

Holwell, B. D. & McDonald, I. (2010). A review of the behaviour of platinum group elements within natural magmatic sulfide ore systems. *Platinum Metals Review* **54**, 26-36. https://doi.org/10.1595/147106709X480913

Huang, H.-H., Lin, F.-C., Schmandt, B., Farrell, J., Smith, R. B. & Tsai, V. C. (2015). The Yellowstone magmatic system from the mantle plume to the upper crust. *Science* **348**, 773-776. https://doi.org/10.1126/science.aaa5648

Huber, C., Bachmann, O., Florez, D., Parmentier, E., Peč, M., Latt, J., Rambosson, M. & Das, U. (2025a). The Mechanics of Multiphase Magmas: A Perspective from the Scale of Crystals and Bubbles to Magma Reservoirs. *Annual Review of Earth and Planetary Sciences* **54**. https://doi.org/10.1146/annurev-earth-032524-124419

Huber, C., Bachmann, O. & Manga, M. (2009). Homogenization processes in silicic magma chambers by stirring and mushification (latent heat buffering). *Earth and Planetary Science Letters* **283**, 38-47. https://doi.org/10.1016/j.epsl.2009.03.029

Huber, C., Parmentier, E. & Florez, D. (2025b). Particle sedimentation in a fluid at low Reynolds number: A generalization of hindered settling described by a two-phase continuum model. *Geochemistry, Geophysics, Geosystems* **26**, e2024GC011820. https://doi.org/10.1029/2024GC011820

Hughes, G. E., Petrone, C. M., Downes, H., Varley, N. R. & Hammond, S. J. (2021). Mush remobilisation and mafic recharge: a study of the crystal cargo of the 2013–17 eruption at Volcán de Colima, Mexico. *Journal of Volcanology and Geothermal Research* **416**, 107296. https://doi.org/10.1016/j.jvolgeores.2021.107296

Humphreys, M. C., Namur, O., Bohrson, W. A., Bouilhol, P., Cooper, G. F., Cooper, K. M., Huber, C., Lissenberg, C. J., Morgado, E. & Spera, F. J. (2025). Crystal mush processes and crustal magmatism. *Nature Reviews Earth & Environment*, 1-16. https://doi.org/10.1038/s43017-025-00682-x

Huppert, H. E. & Sparks, R. S. J. (1989). Chilled margins in igneous rocks. *Earth and Planetary Science Letters* **92**, 397-405. https://doi.org/10.1016/0012-821X(89)90063-0

Hurst, E. (1997). Renewal report for PL 3842, Co. Louth, reporting period 1995 - 1997. BHP. Available at:

https://secure.decc.gov.ie/goldmine/docpage.html?id1=8348185&id2=10312431&id3=10251473

Iacovino, K. & Till, C. B. (2019). DensityX: A program for calculating the densities of magmatic liquids up to 1,627 C and 30 kbar. *Volcanica* **2**. https://doi.org/10.30909/vol.02.01.0110

Irvine, T. (1980). Magmatic density currents and cumulus processes. *American Journal of Science* **280**, 1-58.

Irvine, T. N. (1970). Heat transfer during solidification of layered intrusions. I. Sheets and sills. *Canadian Journal of Earth Sciences* **7**, 1031-1061. https://doi.org/10.1139/e70-098

Jackson, M., Blundy, J. & Sparks, R. (2018). Chemical differentiation, cold storage and remobilization of magma in the Earth's crust. *Nature* **564**, 405-409. https://doi.org/10.1038/s41586-018-0746-2

Jollands, M. C., Bloch, E. & Müntener, O. (2020). New Ti-in-quartz diffusivities reconcile natural Ti zoning with time scales and temperatures of upper crustal magma reservoirs. *Geology* **48**, 654-657. https://doi.org/10.1130/G47238.1

Kruger, F. & Smart, R. (1987). Diffusion of trace elements during bottom crystallization of double-diffusive convection systems: the magnetitite layers of the Bushveld Complex. *Journal of Volcanology and Geothermal Research* **34**, 133-142. https://doi.org/10.1016/0377-0273(87)90098-9

Kruger, F. J. (2005). Filling the Bushveld Complex magma chamber: lateral expansion, roof and floor interaction, magmatic unconformities, and the formation of giant chromitite, PGE and Ti-V-magnetitite deposits. *Mineralium Deposita* **40**, 451-472. https://doi.org/10.1007/s00126-005-0016-8

Lasaulx, A. V. (1878). XXVIII. Petrographische Skizzen aus Irland. *Mineralogische und petrographische Mitteilungen* **1**, 410-449.

Latypov, R. (2015). Basal reversals in mafic sills and layered intrusions. *Layered intrusions*: Springer, 259-293. https://doi.org/10.1007/978-94-017-9652-1_6

Latypov, R., Chistyakova, S., Barnes, S. J., Godel, B., Delaney, G. W., Cleary, P. W., Radermacher, V. J., Campbell, I. & Jakata, K. (2022). Chromitite layers indicate the existence of large, long-lived, and entirely molten magma chambers. *Scientific Reports* **12**, 4092. https://doi.org/10.1038/s41598-022-08110-6

Latypov, R. M., Namur, O., Bai, Y., Barnes, S. J., Chistyakova, S., Holness, M. B., Iacono-Marziano, G., Kruger, W. A., O'Driscoll, B. & Smith, W. D. (2024). Layered intrusions: Fundamentals, novel observations and concepts, and controversial issues. *Earth-Science Reviews* **249**, 104653. https://doi.org/10.1016/j.earscirev.2023.104653

Le Bas, M. J. (1960). VIII.—The Petrology of the Layered Basic Rocks of the Carlingford Complex, Co. Louth. *Earth and Environmental Science Transactions of The Royal Society of Edinburgh* **64**, 169-200. https://doi.org/10.1017/S008045680010016X

Le Bas, M. J. (1965). The contamination of a gabbro by Carboniferous Limestone at Carlingford, Co. Louth. *Mineralogical magazine and journal of the Mineralogical Society* **34**, 292-302. https://doi.org/10.1180/minmag.1965.034.268.25

Le Bas, M. J. (1967). On the origin of the Tertiary granophyres of the Carlingford Complex, Ireland. *Proceedings of the Royal Irish Academy. Section B: Biological, Geological, and Chemical Science*: JSTOR, 325-338.

Le Bas, M. J. (1970). Trace elements in the gabbros, olivines, augites and magnetites of the Carlingford complex, Ireland. *Proceedings of the Royal Irish Academy. Section B: Biological, Geological, and Chemical Science*, 217-243.

Lees, J. M. (2007). Seismic tomography of magmatic systems. *Journal of Volcanology and Geothermal Research* **167**, 37-56. https://doi.org/10.1016/j.jvolgeores.2007.06.008

Lesher, C. E. & Walker, D. (1988). Cumulate maturation and melt migration in a temperature gradient. *Journal of Geophysical Research: Solid Earth* **93**, 10295-10311. https://doi.org/10.1029/JB093iB09p10295

Leuthold, J., Blundy, J. D., Holness, M. B. & Sides, R. (2014). Successive episodes of reactive liquid flow through a layered intrusion (Unit 9, Rum Eastern Layered Intrusion, Scotland). *Contributions to Mineralogy and Petrology* **168**, 1-27. https://doi.org/10.1007/s00410-014-1021-7

Maclennan, J. (2019). Mafic tiers and transient mushes: evidence from Iceland. *Philosophical Transactions of the Royal Society A: Mathematical, Physical and Engineering Sciences* **377**. https://doi.org/10.1098/rsta.2018.0021

Marsh, B. (2004). A magmatic mush column rosetta stone: the McMurdo Dry Valleys of Antarctica. *Eos, Transactions American Geophysical Union* **85**, 497-502. https://doi.org/10.1029/2004EO470001

Marsh, B. D. (1996). Solidification fronts and magmatic evolution. *Mineralogical Magazine* **60**, 5-40. https://doi.org/10.1180/minmag.1996.060.398.03

McBirney, A. R. (1985). Further considerations of double-diffusive stratification and layering in the Skaergaard intrusion. *Journal of Petrology* **26**, 993-1001. https://doi.org/10.1093/petrology/26.4.993

McBirney, A. R. & Noyes, R. M. (1979). Crystallization and Layering of the Skaergaard Intrusion*. *Journal of Petrology* **20**, 487-554. https://doi.org/10.1093/petrology/20.3.487

Meade, F. C. (2008). Processes of Magmatic Differentiation withing the Southern British and Irish PalaeogeneIgneous Province (PhD thesis). *Department of Geology*: University of Dublin, Trinity College.

Meade, F. C., Troll, V. R., Ellam, R. M., Freda, C., Font, L., Donaldson, C. H. & Klonowska, I. (2014). Bimodal magmatism produced by progressively inhibited crustal assimilation. *Nature communications* **5**, 4199. https://doi.org/10.1038/ncomms5199

Mitchell, W. I., Cooper, M. R., Hards, V. L. & Meighan, I. G. (1999). An occurrence of silicic volcanic rocks in the early Palaeogene Antrim Lava Group of Northern Ireland. *Scottish Journal of Geology* **35**, 179-185. https://doi.org/10.1144/sjg35020179

Mulligan, S. (1983). Diamond drill hole log 676/5 PL's 676, 1552 and 1553 Total depth 421' (5 pgs. including assay). Available at: https://secure.decc.gov.ie/goldmine/docpage.html?id1=8327385&id2=10261949&id3=10231329

Mungall, J. E., Kamo, S. L. & McQuade, S. (2016). U–Pb geochronology documents out-of-sequence emplacement of ultramafic layers in the Bushveld Igneous Complex of South Africa. *Nature communications* **7**, 13385. https://doi.org/10.1038/ncomms13385

Mungall, J. E. & Naldrett, A. J. (2008). Ore deposits of the platinum-group elements. *Elements* **4**, 253-258. https://doi.org/10.2113/GSELEMENTS.4.4.253

Mussett, A. E., Dagley, P. & Skelhorn, R. R. (1988). Time and duration of activity in the British Tertiary Igneous Province. *Geological Society, London, Special Publications* **39**, 337-348. https://doi.org/10.1144/GSL.SP.1988.039.01.29

Nakagawa, M., Wada, K. & Wood, C. P. (2002). Mixed magmas, mush chambers and eruption triggers: evidence from zoned clinopyroxene phenocrysts in andesitic scoria from the 1995 eruptions of Ruapehu volcano, New Zealand. *Journal of Petrology* **43**, 2279-2303. https://doi.org/10.1093/petrology/43.12.2279

Namur, O., Abily, B., Boudreau, A. E., Blanchette, F., Bush, J. W., Ceuleneer, G., Charlier, B., Donaldson, C. H., Duchesne, J.-C. & Higgins, M. D. (2015). Igneous layering in basaltic magma chambers. *Layered intrusions*: Springer, 75-152. https://doi.org/10.1007/978-94-017-9652-1_2

Namur, O., Charlier, B., Toplis, M. J., Higgins, M. D., Liégeois, J.-P. & Vander Auwera, J. (2010). Crystallization sequence and magma chamber processes in the ferrobasaltic Sept Iles layered intrusion, Canada. *Journal of Petrology* **51**, 1203-1236. https://doi.org/10.1093/petrology/egq016

Neave, D. A., Buisman, I. & Maclennan, J. (2017). Continuous mush disaggregation during the long-lasting Laki fissure eruption, Iceland. *American Mineralogist* **102**, 2007-2021. https://doi.org/10.2138/am-2017-6015CCBY

Nielsen, T. F. (2004). The shape and volume of the Skaergaard intrusion, Greenland: implications for mass balance and bulk composition. *Journal of Petrology* **45**, 507-530. https://doi.org/10.1093/petrology/egg092

Nockolds, S. R. (1935). Contributions to the Petrology of Barnavave, Carlingford, IFS—1. The Junction Hybrids. *Geological Magazine* **72**, 289-315. https://doi.org/10.1017/S0016756800094292

Nockolds, S. R. & Mitchell, R. L. (1944). Contributions to the Petrology of Barnavave, Carlingford, IFS—4. Some Limestone Xenoliths enclosed in the Junction Hybrids. *Geological Magazine* **81**, 88-94. https://doi.org/10.1017/S0016756800074033

Nockolds, S. R. & Vincent, H. G. C. (1947). On tilleyite and its associated minerals from Carlingford, Ireland (With Plates XI and XII.). *Mineralogical magazine and journal of the Mineralogical Society* **28**, 151-158. https://doi.org/10.1180/minmag.1947.028.198.04

O'Connor, P. J. (1990). Strontium isotope compositions of acid-basic magma associations in the Tertiary intrusive centres of NE Ireland. *Geological Survey of Ireland Bulletin* **4**, 227-243.

O'Driscoll, B. (2006). Magmatic layering and magnetic fabrics in the Palaeogene Carlingford Later Gabbros, Co. Louth, Ireland. *Irish Journal of Earth Sciences* **24**, 37-50. https://doi.org/10.1353/ijes.2006.0001

O'Driscoll, B. & VanTongeren, J. A. (2017). Layered intrusions: from petrological paradigms to precious metal repositories. *Elements: An International Magazine of Mineralogy, Geochemistry, and Petrology* **13**, 383-389. https://doi.org/10.2138/gselements.13.6.383

Osborne, G. D. (1932). The Metamorphosed Limestones and Associated Contaminated Igneous Rocks of the Carlingford District, Co. Louth. *Geological Magazine* **69**, 209-233. https://doi.org/10.1017/S0016756800097223

Paulatto, M., Annen, C., Henstock, T. J., Kiddle, E., Minshull, T. A., Sparks, R. & Voight, B. (2012). Magma chamber properties from integrated seismic tomography and thermal modeling at Montserrat. *Geochemistry, Geophysics, Geosystems* **13**. https://doi.org/10.1029/2011GC003892

Paulatto, M., Hooft, E. E., Chrapkiewicz, K., Heath, B., Toomey, D. R. & Morgan, J. V. (2022). Advances in seismic imaging of magma and crystal mush. *Frontiers in Earth Science* **10**, 970131. https://doi.org/10.3389/feart.2022.970131

Renner, R. & Palacz, Z. (1987). Basaltic replenishment of the Rhum magma chamber: evidence from unit 14. *Journal of the Geological Society* **144**, 961-970. https://doi.org/10.1144/gsjgs.144.6.0961

Richardson, J. & Zaki, W. (1954). The sedimentation of a suspension of uniform spheres under conditions of viscous flow. *Chemical Engineering Science* **3**, 65-73. https://doi.org/10.1016/0009-2509(54)85015-9

Richey, J. E. (1932). II.—Tertiary Ring Structures in Britain. *Transactions of the Geological Society of Glasgow* **19**, 42-140. https://doi.org/10.1144/transglas.19.1.42

Robie, R. A., Beardsley, K. M. & Bethke, P. M. (1967). *Selected X-ray crystallographic data, molar volumes, and densities of minerals and related substances*: US Government Printing Office.

Roduit, N. (2007). *JMicroVision: un logiciel d'analyse d'images pétrographiques polyvalent*: Section des Sciences de la Terre, Université de Genève.

Roman, A. & Jaupart, C. (2016). The fate of mafic and ultramafic intrusions in the continental crust. *Earth and Planetary Science Letters* **453**, 131-140. https://doi.org/10.1016/j.epsl.2016.07.048

Rudnick, R. L. (1995). Making continental crust. *Nature* **378**, 571-578. https://doi.org/10.1038/378571a0

Sajjadi, S., Martinec, Z., Prendergast, P., Hagedoorn, J., Šachl, L., Readman, P., Edwards, R., O'Reilly, B. & Horan, C. (2020). The unification of gravity data for Ireland-Northern Ireland. *The Leading Edge* **39**, 135-143. https://doi.org/10.1190/tle39020135.1

Saunders, A. D., Fitton, J. G., Kerr, A. C., Norry, M. J., Kent, R. W., Mahoney, J. J. & Coffin, M. F. (1997). The north Atlantic igneous province. *Geophysical Monograph-American Geophysical Union* **100**, 45-94. https://doi.org/10.1029/GM100p0045

Schauroth, J., Burchardt, S., Meade, F. & Troll, V. R. (2014). 3D cone-sheet and crystal-settling models reveal magma-reservoir structure of the Carlingford central complex, Ireland. *EGU General Assembly Conference Abstracts*, 5783.

Schneider, C. A., Rasband, W. S. & Eliceiri, K. W. (2012). NIH Image to ImageJ: 25 years of image analysis. *Nature methods* **9**, 671-675. https://doi.org/10.1038/nmeth.2089

Sollas, W. J. (1892). On the volcanic district of Carlingford and Slieve Gullion. Part I.: On the Relation of the Granite to the Gabbro of Barnavave, Carlingford. *The Transactions of the Royal Irish Academy* **30**, 477-512.

Sparks, R., Annen, C., Blundy, J., Cashman, K., Rust, A. & Jackson, M. (2019). Formation and dynamics of magma reservoirs. *Philosophical Transactions of the Royal Society A: Mathematical, Physical and Engineering Sciences* **377**. https://doi.org/10.1098/rsta.2018.0019

Stickels, C. A. & Hücke, E. E. (1964). Measurement of dihedral angles. *Transactions of the Metallurgical Society of AIME* **230**, 795-801.

Stock, M. J., Geist, D., Neave, D. A., Gleeson, M. L., Bernard, B., Howard, K. A., Buisman, I. & Maclennan, J. (2020). Cryptic evolved melts beneath monotonous basaltic shield volcanoes in the Galápagos Archipelago. *Nature communications* **11**, 3767. https://doi.org/10.1038/s41467-020-17590-x

Tegner, C., Cawthorn, R. G. & Kruger, F. J. (2006). Cyclicity in the Main and Upper Zones of the Bushveld Complex, South Africa: crystallization from a zoned magma sheet. *Journal of Petrology* **47**, 2257-2279. https://doi.org/10.1093/petrology/egl043

Thompson, P. (1985). Dating the British Tertiary Igneous Province in Ireland by the 40Ar-39Ar stepwise degassing method. University of Liverpool.

Thy, P., Tegner, C. & Lesher, C. E. (2023). Petrology of the Skaergaard layered series. *GEUS Bulletin* **56**. https://doi.org/10.34194/geusb.v56.8327

Traill, W. A. (1878). Explanatory Memoir to accompany Part of Sheets 60 and 71 of the Maps of the Geological Survey of Ireland. *Mem. Geol. Surv*.

Vukmanovic, Z., Holness, M., Monks, K. & Andersen, J. Ø. (2018). The Skaergaard trough layering: sedimentation in a convecting magma chamber. *Contributions to Mineralogy and Petrology* **173**, 43. https://doi.org/10.1007/s00410-018-1466-1

Wager, L. R. & Brown, G. M. (1968). *Layered Igneous Rocks*. Edinburgh: Oliver & Boyd.

Wager, L. R. & Deer, W. A. (1939). Geological investigations in East Greenland. Part III. The petrology of the Skaergaard intrusion, Kangerdlugssuag, East Geenland. *Meddelelser om Grønland* **105**, 1-352.

Wall, C. J., Scoates, J. S., Weis, D., Friedman, R. M., Amini, M. & Meurer, W. P. (2018). The Stillwater Complex: integrating zircon geochronological and geochemical constraints on the age, emplacement history and crystallization of a large, open-system layered intrusion. *Journal of Petrology* **59**, 153-190. https://doi.org/10.1093/petrology/egy024

Ward, K. M., Zandt, G., Beck, S. L., Christensen, D. H. & McFarlin, H. (2014). Seismic imaging of the magmatic underpinnings beneath the Altiplano-Puna volcanic complex from the joint inversion of surface wave dispersion and receiver functions. *Earth and Planetary Science Letters* **404**, 43-53. https://doi.org/10.1016/j.epsl.2014.07.022

Wilkinson, C. M., Ganerød, M., Hendriks, B. W. & Eide, E. A. (2017). Compilation and appraisal of geochronological data from the North Atlantic Igneous Province (NAIP). https://doi.org/10.1144/SP447.10

Wotzlaw, J.-F., Bindeman, I. N., Schaltegger, U., Brooks, C. K. & Naslund, H. R. (2012). High-resolution insights into episodes of crystallization, hydrothermal alteration and remelting in the Skaergaard intrusive complex. *Earth and Planetary Science Letters* **355**, 199-212. https://doi.org/10.1016/j.epsl.2012.08.043

Yao, Z., Mungall, J. E. & Jenkins, M. C. (2021). The Rustenburg Layered Suite formed as a stack of mush with transient magma chambers. *Nature communications* **12**, 505. https://doi.org/10.1038/s41467-020-20778-w

Young, M. & Donald, A. (2013). *A guide to the Tellus data*: Geological Survey of Northern Ireland.

Zientek, M. L. (2012). Magmatic ore deposits in layered intrusions: Descriptive model for reef-type PGE and contact-type Cu-Ni-PGE deposits. https://doi.org/10.3133/ofr20121010

TABLES AND FIGURES

Table 1: Summary of the new stratigraphic sub-divisions of the Later Gabbros.

Reclassified zone (this paper)	Former layer classification (Le Bas, 1960)	Height of base above MZ (m)	Thickness (m)	No. samples	Sampling transects
UZB	E4	411	>145 (upper contact not preserved)	14	N Foye
UZA	E3	300	115	27	N Foye SE Foye
MZ	E2 E1	0	317	28	N Foye SE Foye Core (up to 3 m)
LZ (Subzones C1-C11)		-93	94	41	Core N Foye (up to -8 m) SE Foye (up to -44 m)

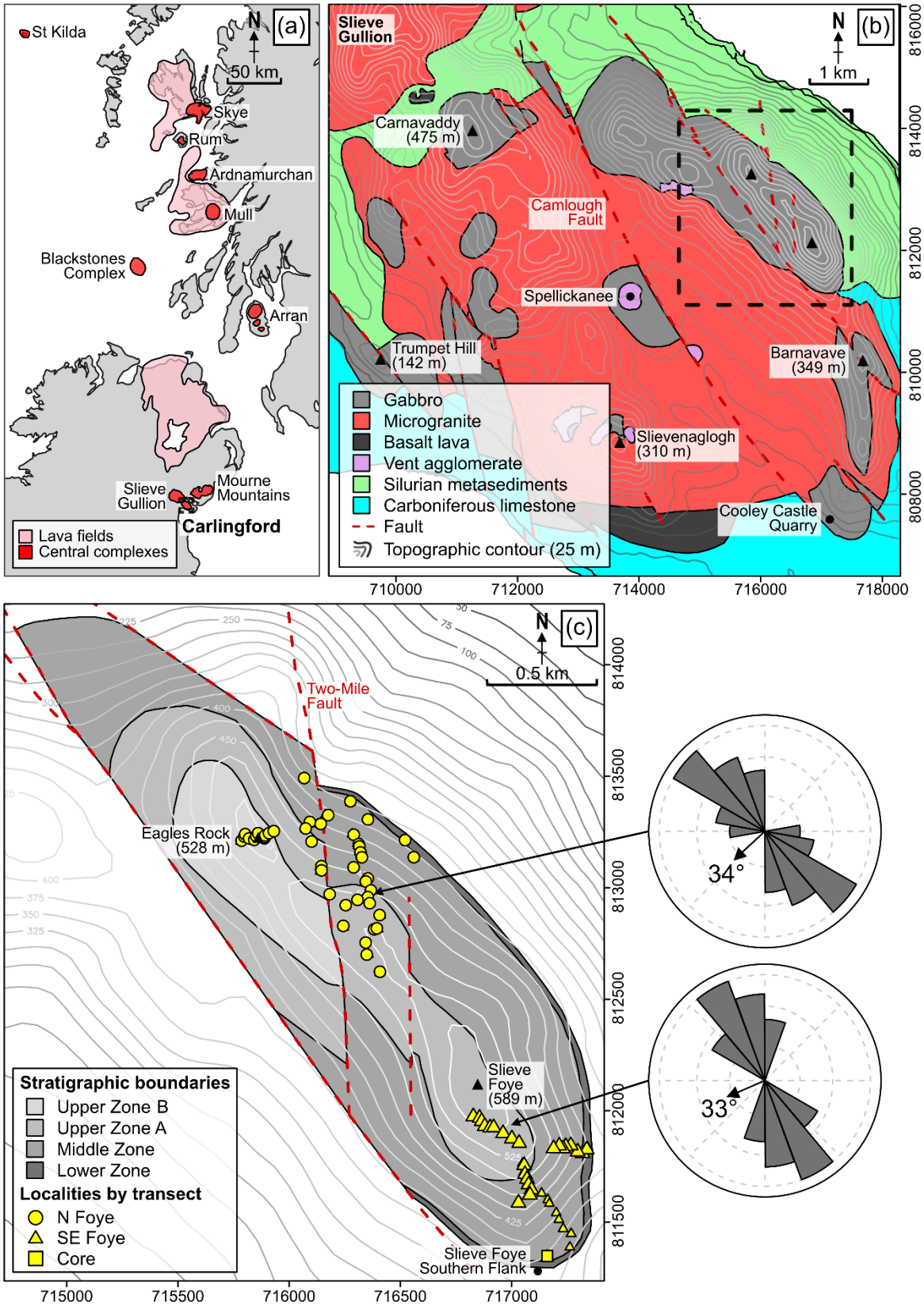

Figure 1: (a) Map of the major lava fields and central complexes of the BIPIP. Adapted from Cooper (2004) and Emeleus and Bell (2005). **(b)** Topographic geological map of the Carlingford Complex, modified after Richey (1932) and Le Bas (1960). The black dashed box

indicates the area of detailed study at Slieve Foye. **(c)** Positions of sampling localities within the layered gabbros at Slieve Foye (within the dashed box in b). Stratigraphic boundaries were reinterpreted from Le Bas (1960) to fit our new stratigraphic characterisation [see Discussion]. Rose diagrams show the orientation and average dip direction (black arrows) of layering surfaces along the North and Southeast Foye transects. Black triangles represent hill peaks and black circles named locations mentioned in the main text. See Supplementary Table 1 for sampling coordinates.

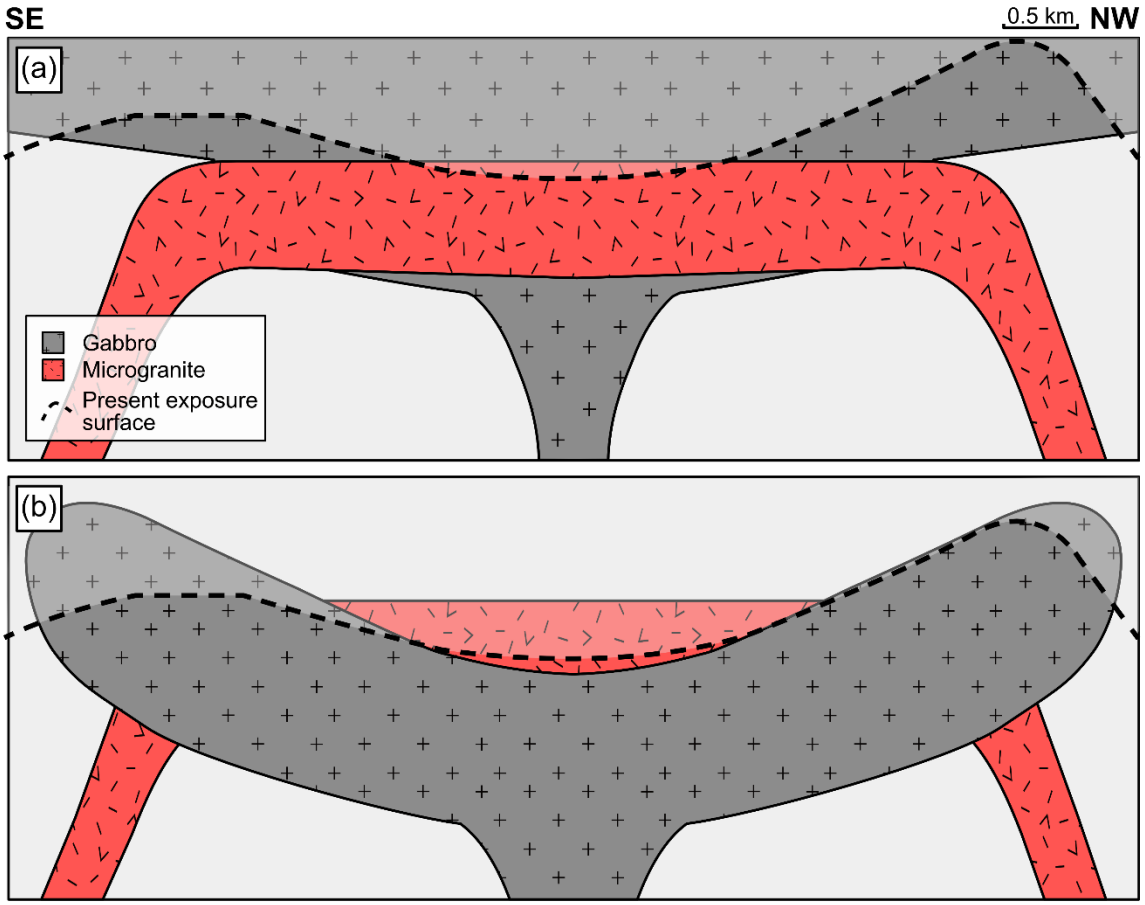

Figure 2: Schematic cross sections of the Carlingford Complex showing contrasting interpretations of the relationship between the gabbro and microgranite ring dyke. **(a)** Gabbro intruded prior to the microgranite, with a sub-horizontal basal contact (modified after Le Bas, 1960, Le Bas, 1970). **(b)** Gabbro intruded as an inward-dipping lopolith after the emplacement of the granophyre (modified after Meade, 2008, Meade *et al.*, 2014).

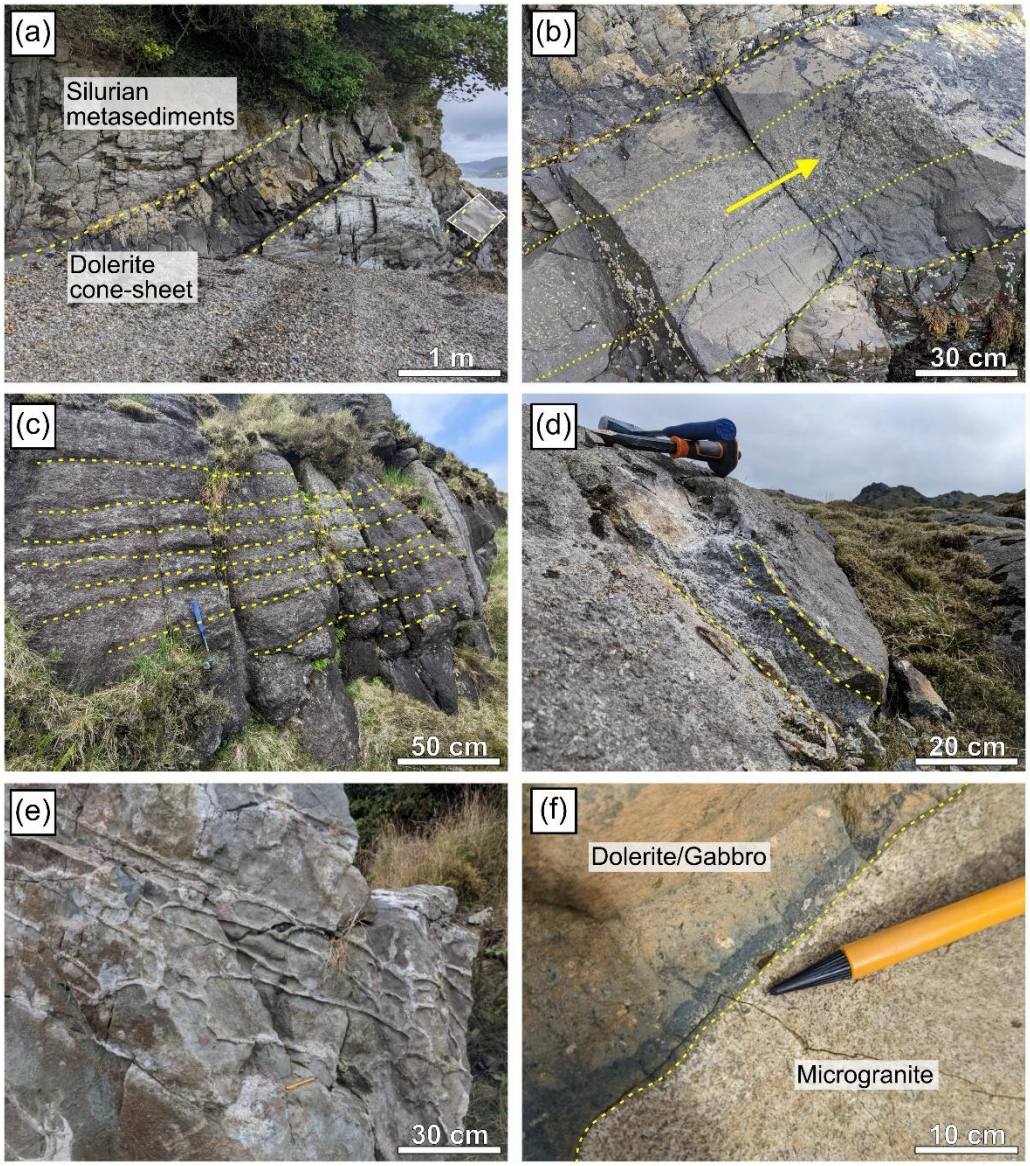

Figure 3: Photographs of field features. **(a)** Cone-sheets intruded within Silurian metasediments (dipping W towards centre of Carlingford Complex, outlined with dashed lines). **(b)** Close-up of highlighted plagioclase-phyric cone sheet outlined in (a), showing central concentration of phenocrysts due to Bagnold flow (outlined by dotted lines; yellow arrow marks possible flow direction). **(c)** Small-scale magmatic layering in the MZ, shown by dotted lines. **(d)** Layer-parallel mafic intrusion within more felsic gabbro in UZA (dipping SW towards centre of Carlingford Complex). **(e)** Microgranite back-veining of dolerite in the Cooley Castle Quarry, indicative of a younger age of the mafic rocks **(f)** Chilled dolerite at the contact with recrystallised microgranite at Cooley Castle Quarry.

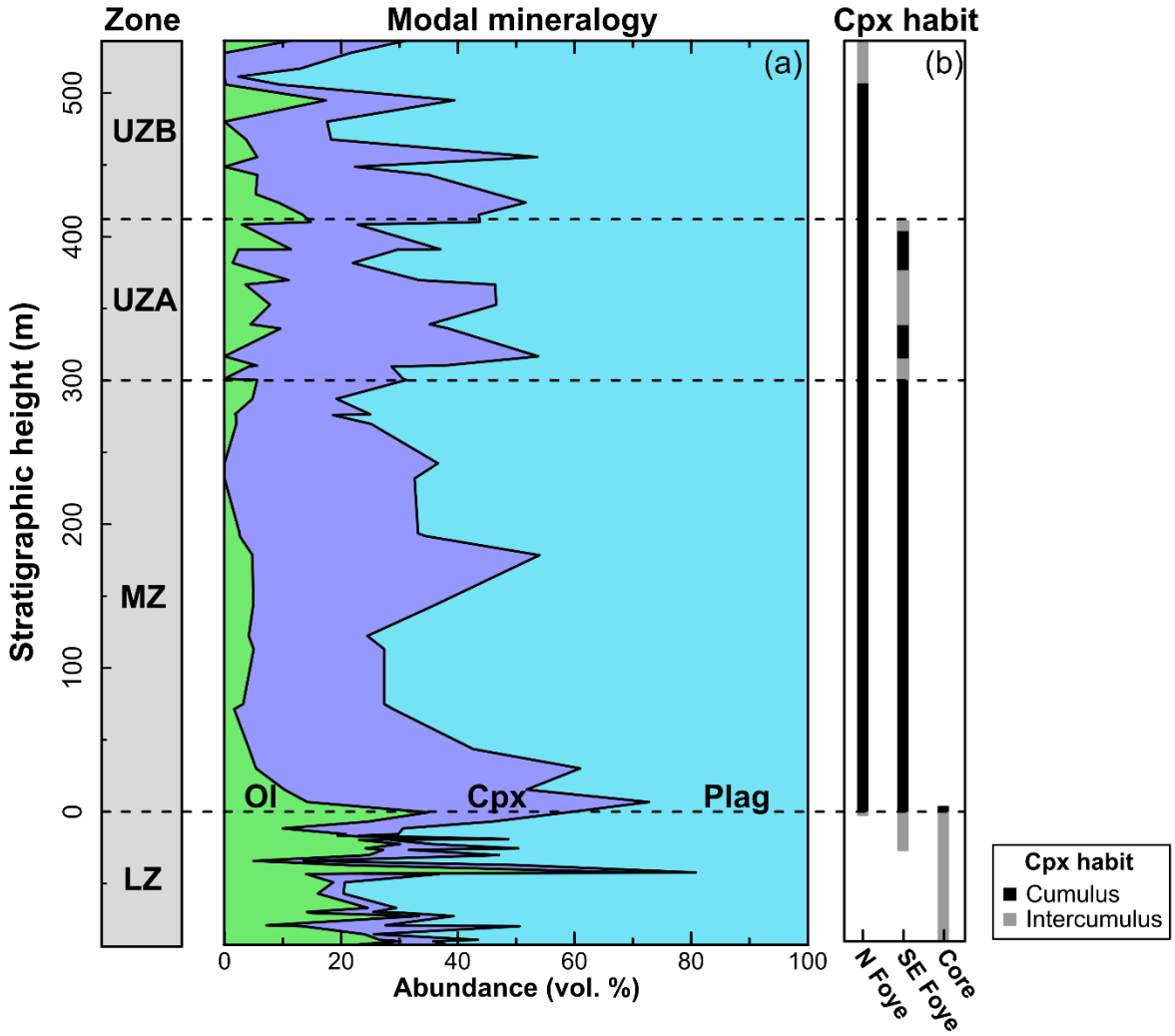

Figure 4: Overview stratigraphic variations in **(a)** modal abundances, determined by random grid point counting, of olivine (Ol), clinopyroxene (Cpx), and plagioclase (Plag), normalised to 100%, and **(b)** clinopyroxene habit in each of the three transects, shown as cumulus (black) or intercumulus (light grey). Revised stratigraphic subdivisions are shown in the left-hand column.

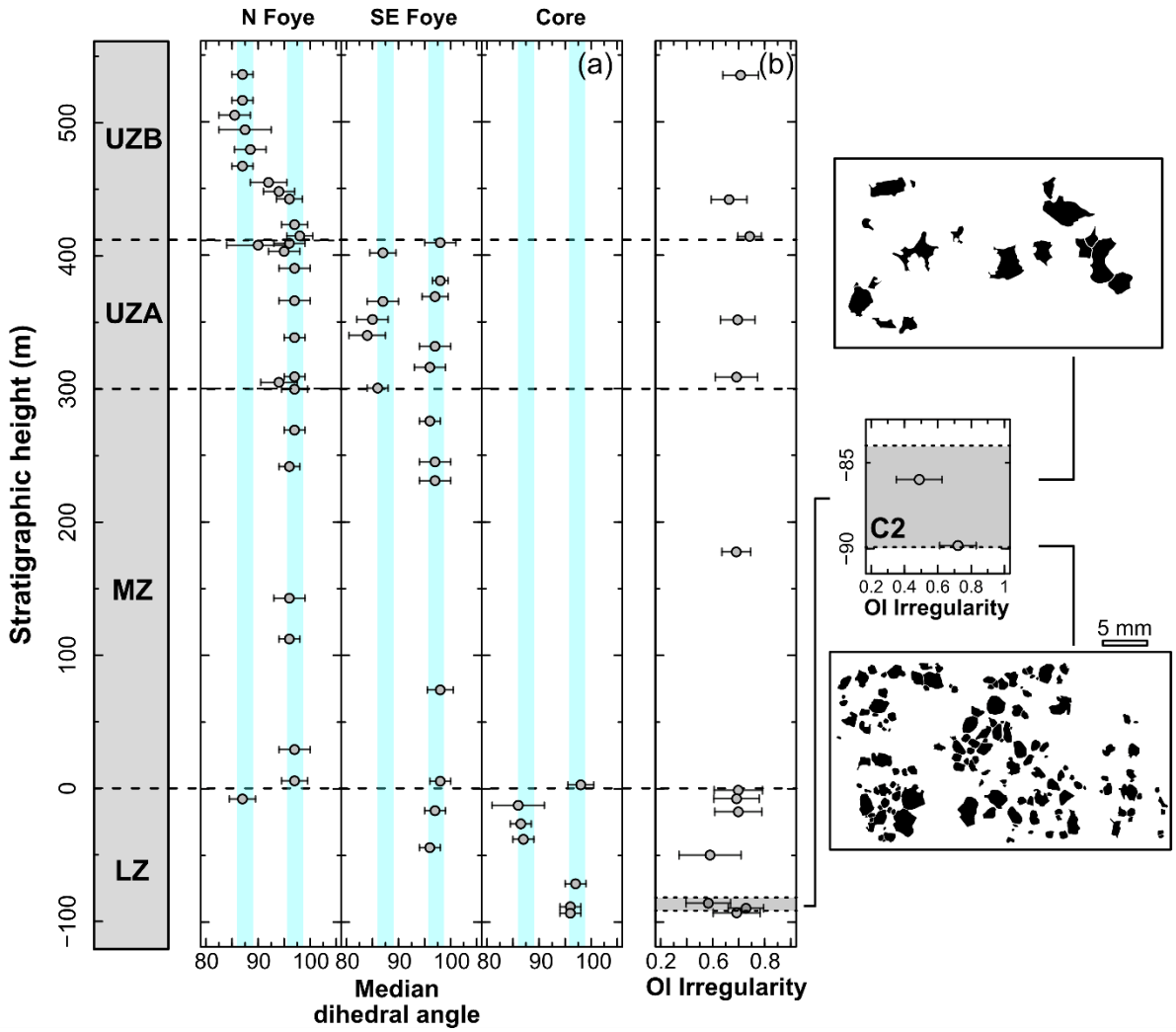

Figure 5: Microstructural variations with stratigraphy. **(a)** Median clinopyroxene-plagioclase-plagioclase dihedral angle (Θ_{cpp}). Θ_{cpp} is bimodal and correlates with the liquidus phase assemblage (cf. Fig. 4): low values indicate bulk magma saturation in olivine and plagioclase, while high values correspond to the addition of clinopyroxene to the liquidus assemblage. Shaded blue bands show ±3° intervals around the mean low (87°) and high (97°) median values. While Θ_{cpp} is the same in the two traverses in the MZ, that in UZA in Southeast Foye oscillates between the two values instead of being constant at high values as it is in North Foye. **(b)** Olivine irregularity. The departure of olivine morphology from a circle is shown by olivine irregularity (where 1 = circle). The sketches show the outlines of olivine grains illustrating the upwards shift from abundant, euhedral olivines, to fewer, clustered, anhedral grains, within each subdivision of the LZ. Revised stratigraphic subdivisions are shown in the left-hand column.

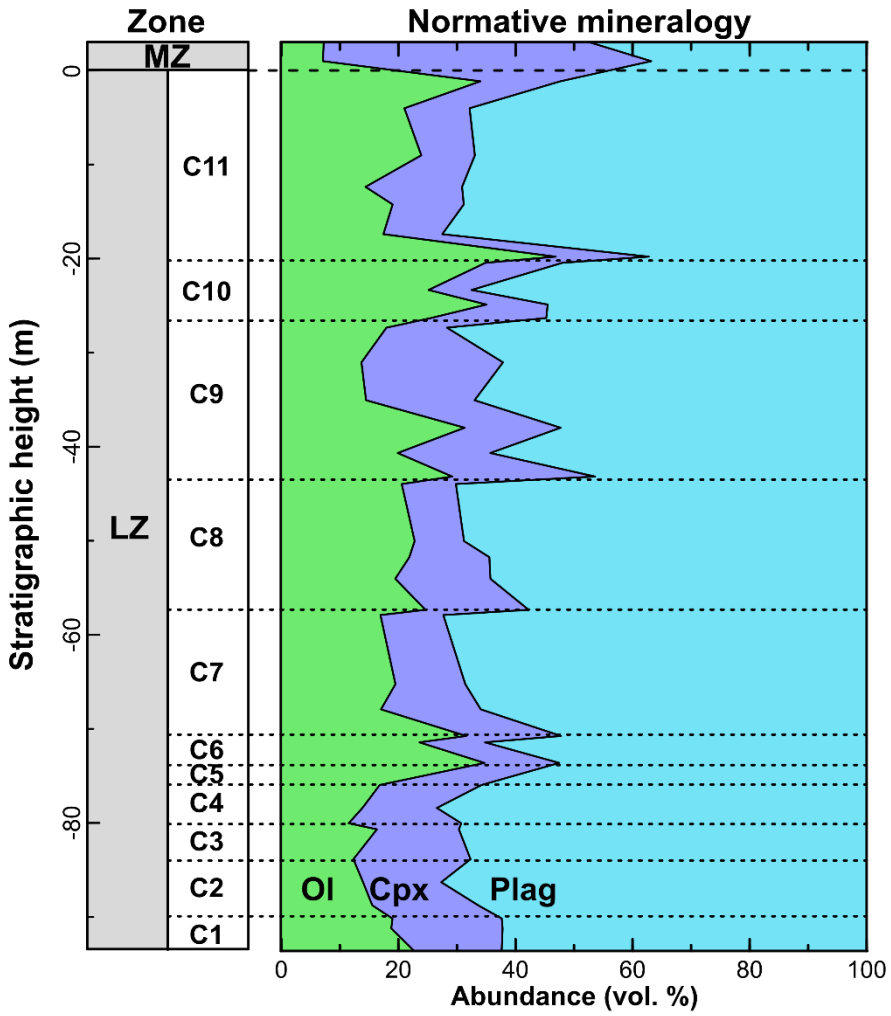

Figure 6: Stratigraphic variations in CIPW normative abundances of olivine, clinopyroxene and plagioclase (abbreviations as in Fig. 4) in the drill core samples of the LZ, normalised to 100%. The individual cyclic units are labelled C1 to C11. Revised stratigraphic subdivisions are shown in the left-hand column.

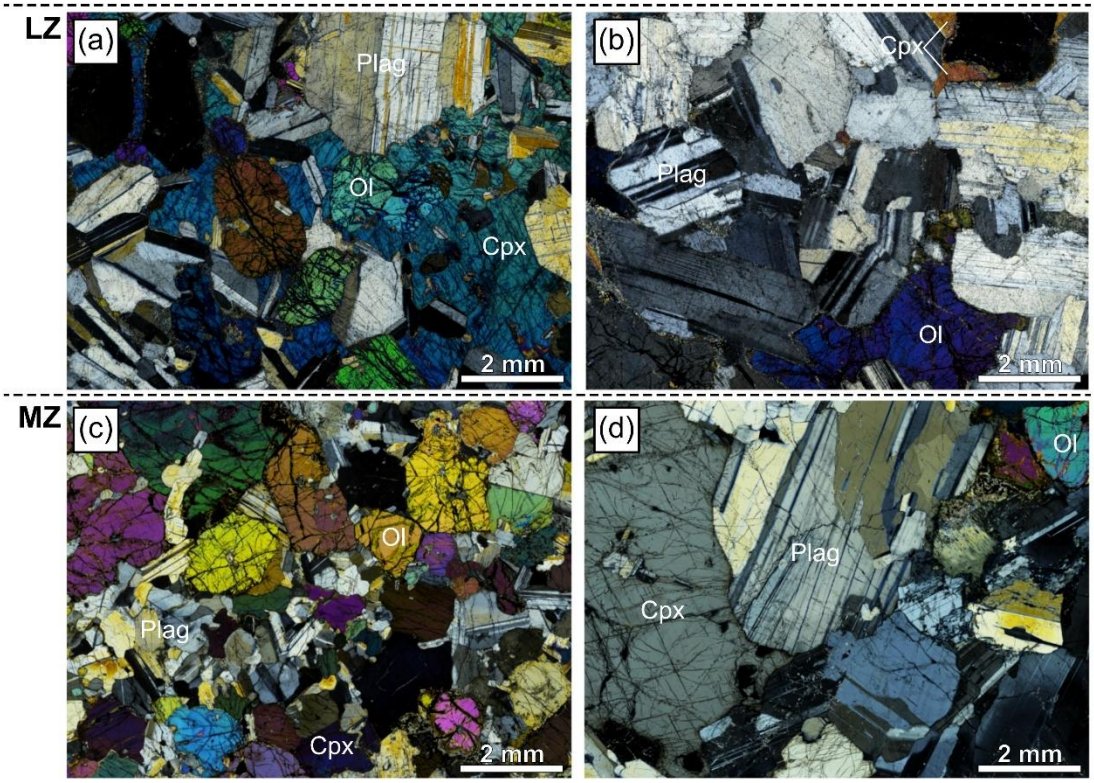

Figure 7: Photomicrographs (under crossed polars) of the Later Gabbros. Abbreviations as in the caption to Fig. 4. **(a)** Abundant olivine primocrysts commonly forming clusters with grains joined on growth faces with poikilitic clinopyroxene, characteristic of the base of most LZ subunits. Plagioclase is generally fine-grained, but with some larger grains. **(b)** Plagioclase-rich gabbro with aspect ratio ~1 and irregular grain boundaries, characteristic of the top of the LZ subunits. **(c)** Abundant euhedral clinopyroxene primocrysts, some with simple twinning, defining the base of the MZ. **(d)** Minor olivine, together with normally-zoned clinopyroxene with extensive interstitial overgrowth at the top of the MZ. Plagioclase forms coarse, low-aspect ratio grains.

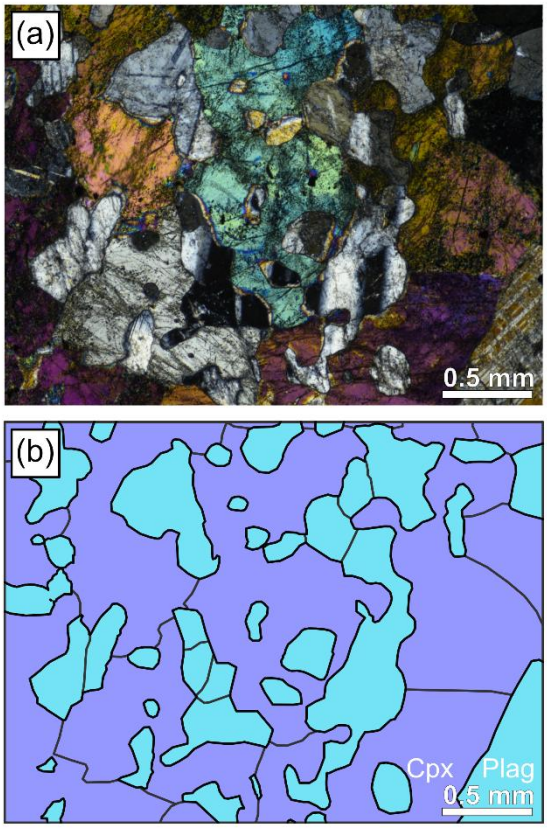

Figure 8: Dendritic clinopyroxenes at the base of the MZ in the drill core. Abbreviations as in the caption to Fig. 4. **(a)** Cross-polarised light. **(b)** Traced grain outlines highlighting the irregular, branched habit of the clinopyroxenes.

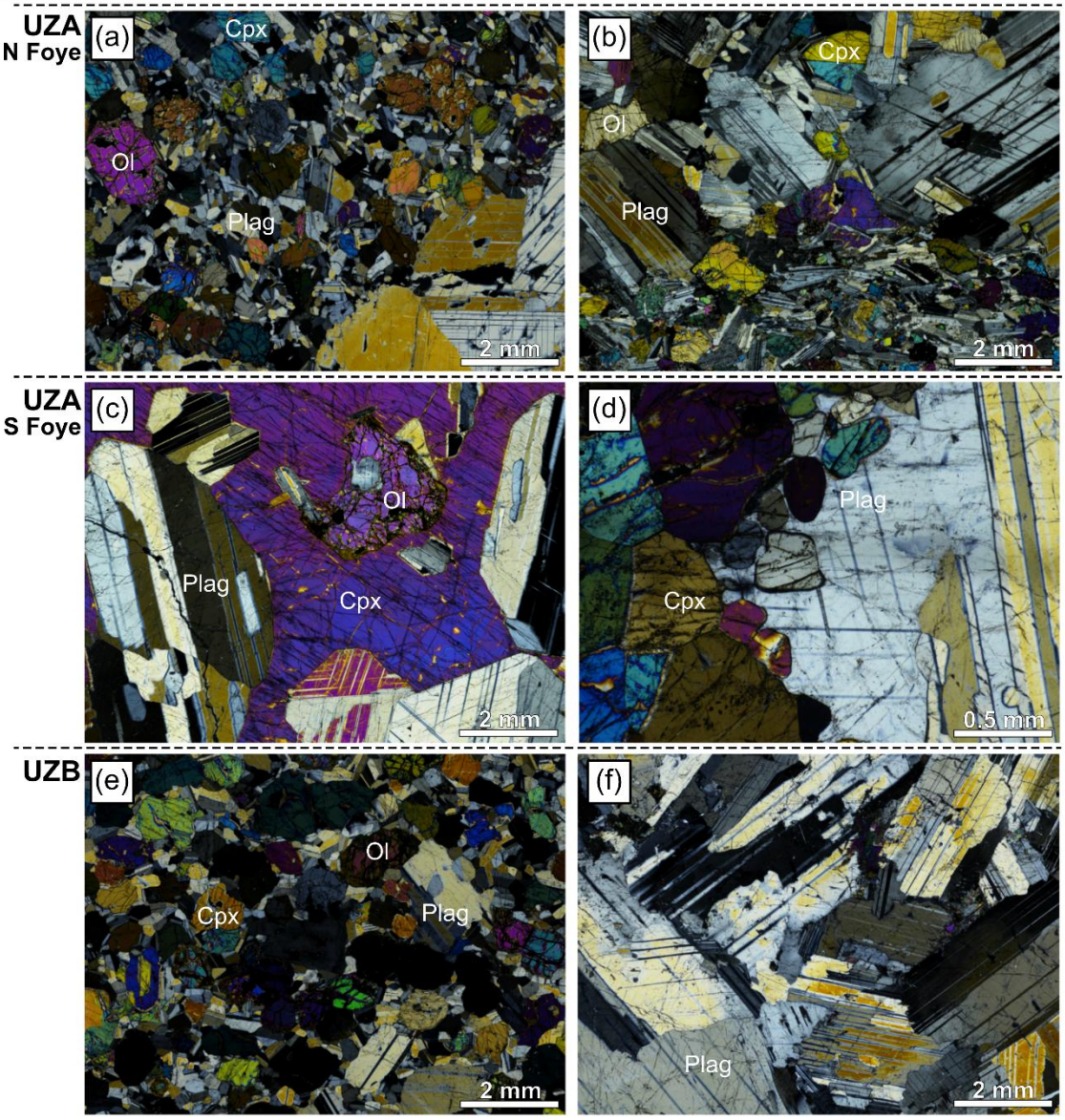

Figure 9: Photomicrographs (under crossed polars) of the Later Gabbros. Abbreviations as in the caption to Fig. 4. **(a)** Rare euhedral olivine, abundant fine-grained euhedral clinopyroxene, together with plagioclase of variable grain size and shape, marking the base of UZA at North Foye. **(b)** Irregular contact between coarse-grained gabbro and a fine-grained gabbro layer with strongly aligned plagioclase laths in UZA at North Foye. **(c)** Euhedral olivine grains and coarse, low aspect ratio plagioclase poikilitically enclosed by abundant clinopyroxene at the base of UZA, Southeast Foye. **(d)** Rounded clinopyroxene primocrysts partially enclosed by plagioclase in UZA at Southeast Foye. **(e)** Fine-grained clusters of idiomorphic olivine and clinopyroxene, together with fine-grained plagioclase at the base of UZB. (f) Anorthosite near the uppermost exposures of UZB.

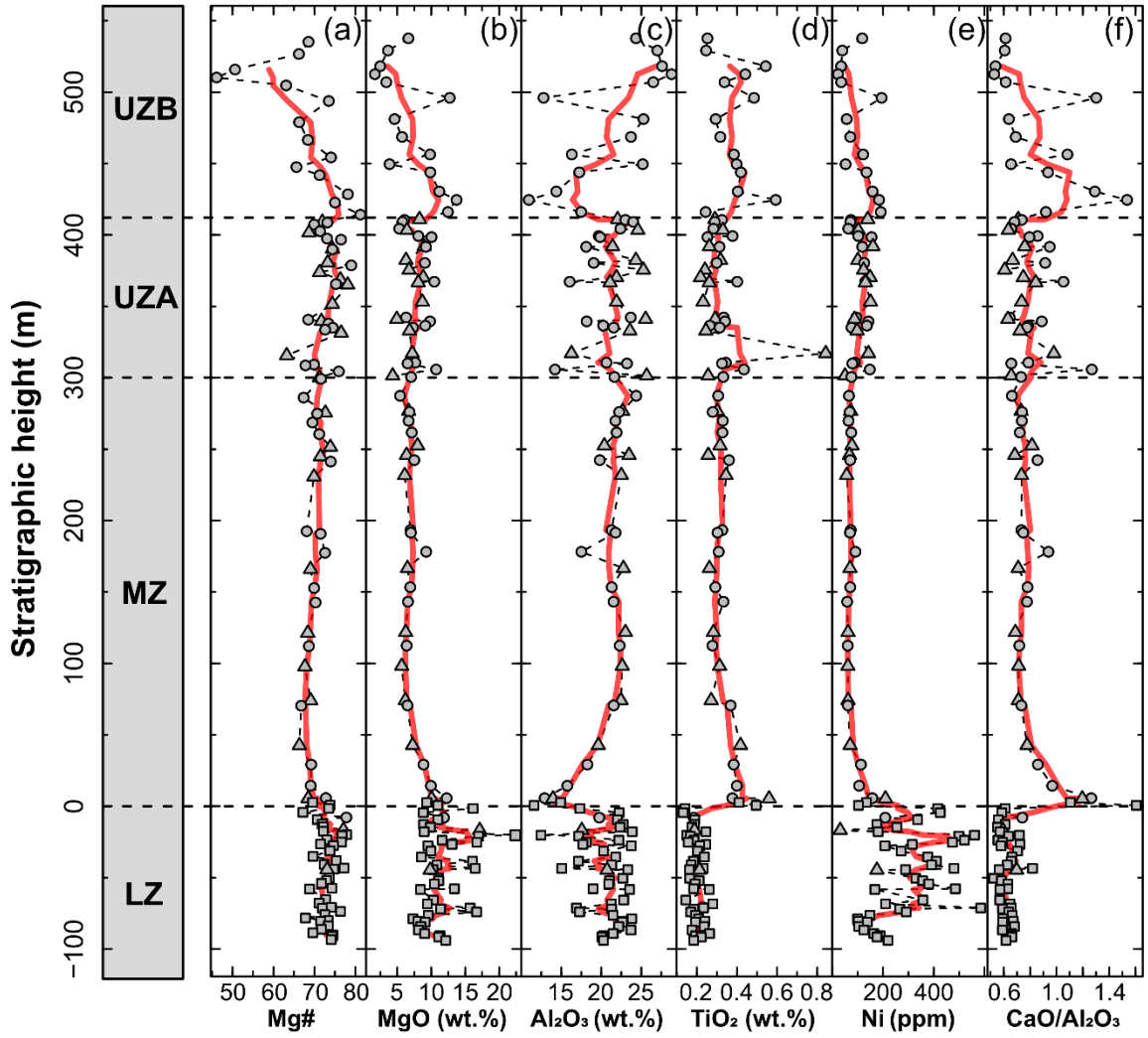

Figure 10. Geochemical variations of selected major and trace elements through the composite stratigraphy. **(a)** Mg#; **(b)** MgO; **(c)** Al_2O_3; **(d)** TiO_2; **(e)** Ni; **(f)** CaO/Al_2O_3. The three different transects are represented by symbols defined in Figure 1c. Red lines represent 5-point rolling means to highlight broader stratigraphic trends.

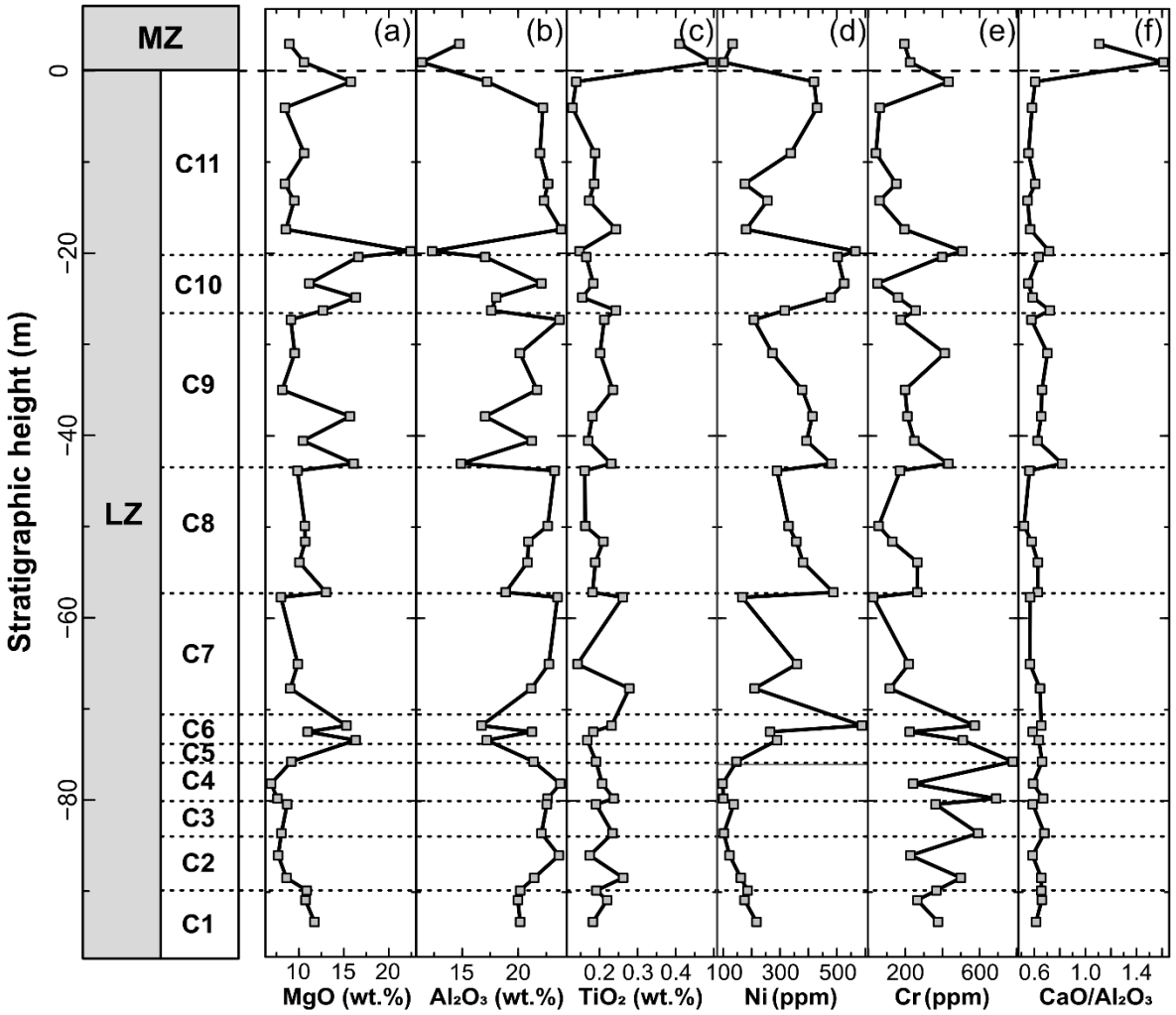

Figure 11: Stratigraphic variation of selected major and trace elements through the LZ (drill core samples only). **(a)** MgO; **(b)** $Al2O_3$; **(c)** TiO_2; **(d)** Ni; **(e)** Cr; **(f)** CaO/Al_2O_3. Revised stratigraphic subdivisions are shown in the left-hand column.

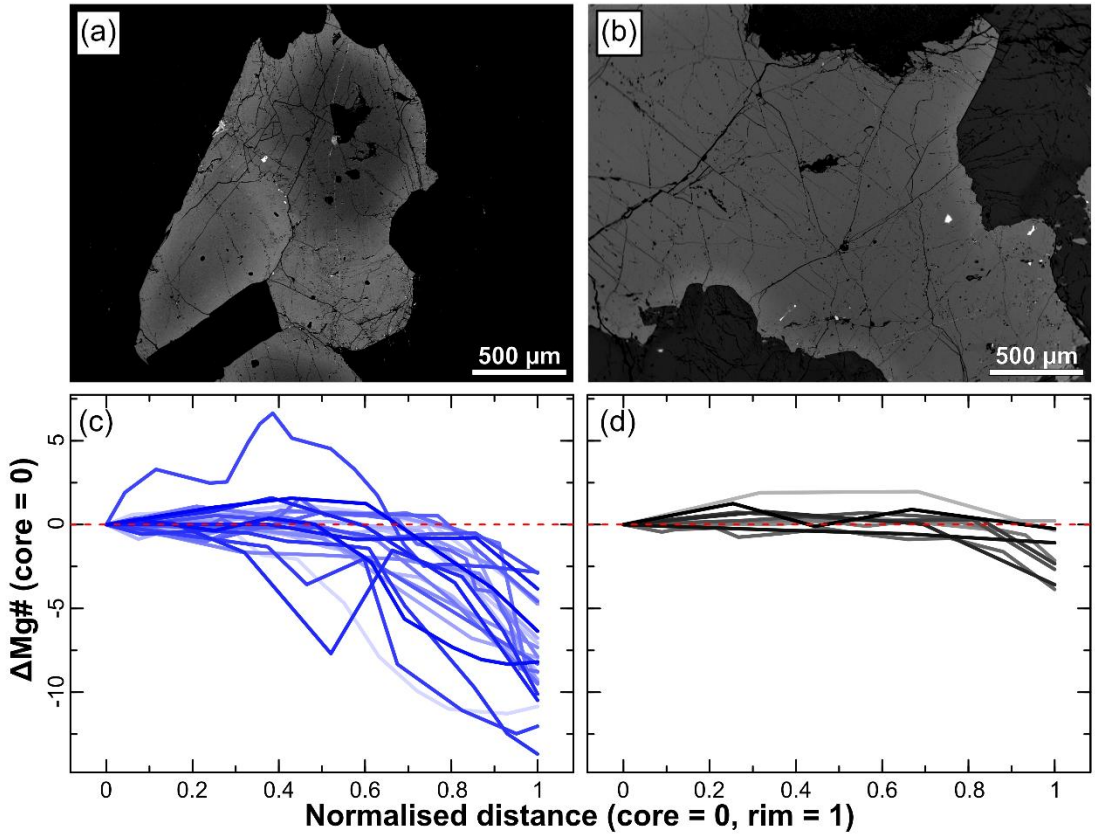

Figure 12: Compositional zoning in **(a)** cumulus and **(b)** intercumulus clinopyroxene shown in backscattered electron (BSE) images. **(c)** Normalised EPMA core to rim traverses (0 = core, 1 = rim) of selected cumulus and **(d)** intercumulus grains, showing normal zoning in Mg# in the outer ~20% of the grains.

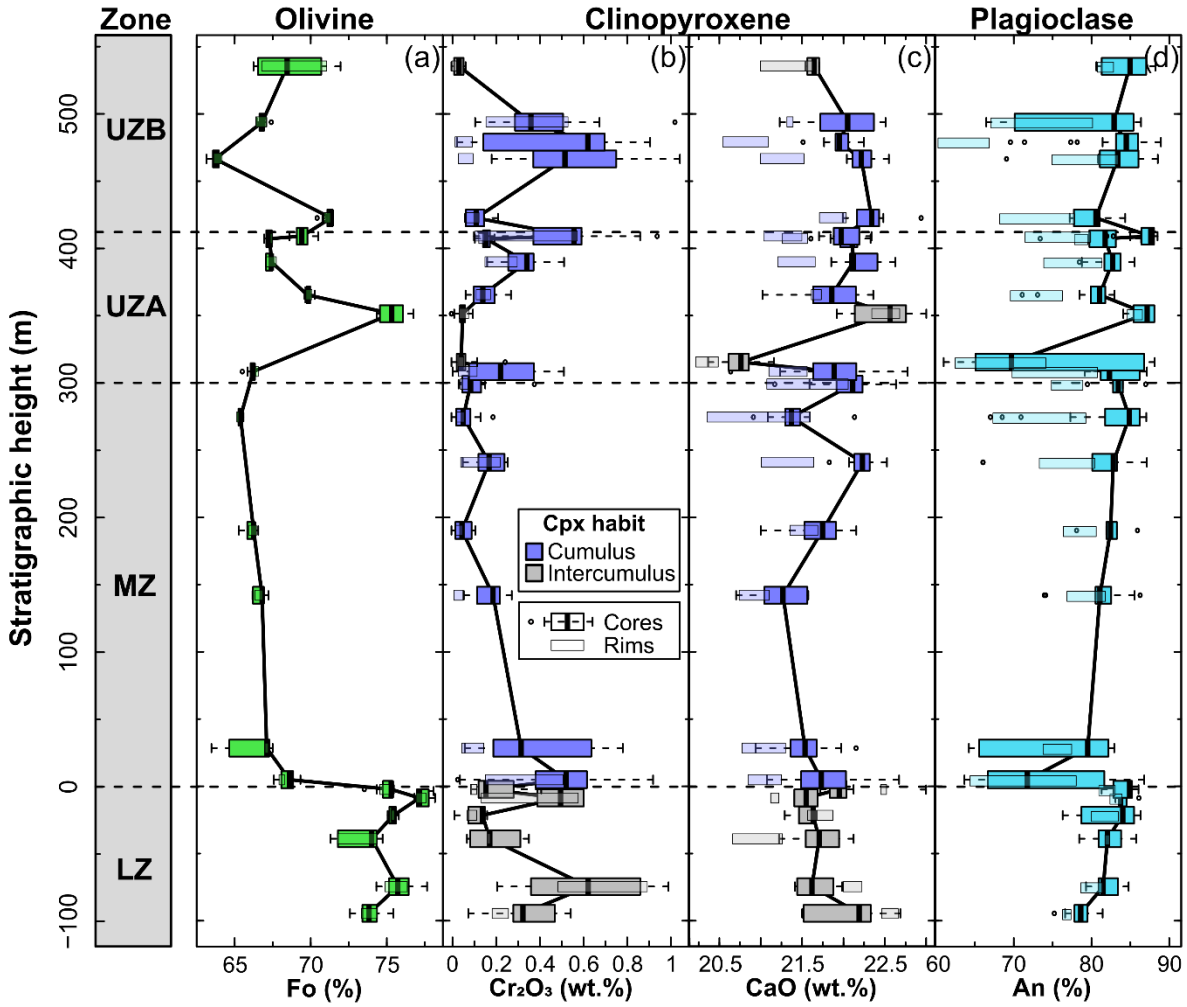

Figure 13: Stratigraphic variation in the composition of olivine (green), clinopyroxene (purple) and plagioclase (blue). **(a)** Olivine Fo; **(b)** clinopyroxene Cr_2O_3; **(c)** clinopyroxene CaO; **(d)** plagioclase An. Boxes show interquartile range (IQR), vertical lines medians, whiskers 1.5× IQR, and points outliers. Core compositions are shown as bold boxplots; rim IQRs are indicated by lighter coloured boxes. Black lines connect median core values through stratigraphy. Revised stratigraphic subdivisions are shown in the left-hand column.

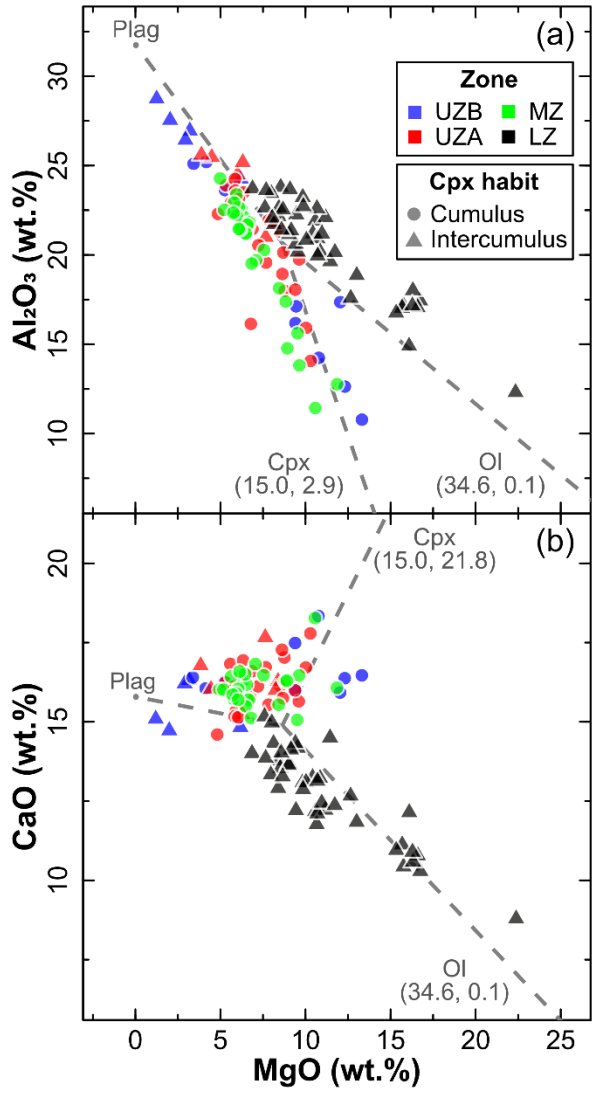

Figure 14: Harker diagrams showing the mineralogical control on gabbro bulk-rock compositions, permitting identification of the primocryst phase assemblage. **(a)** Al_2O_3 vs MgO; **(b)** CaO vs MgO. Mineral poles (abbreviations as in Fig. 4) extend from a central point representing the mean gabbro bulk composition towards the compositions representative of the mean composition of grain cores of the three major mineral phases.

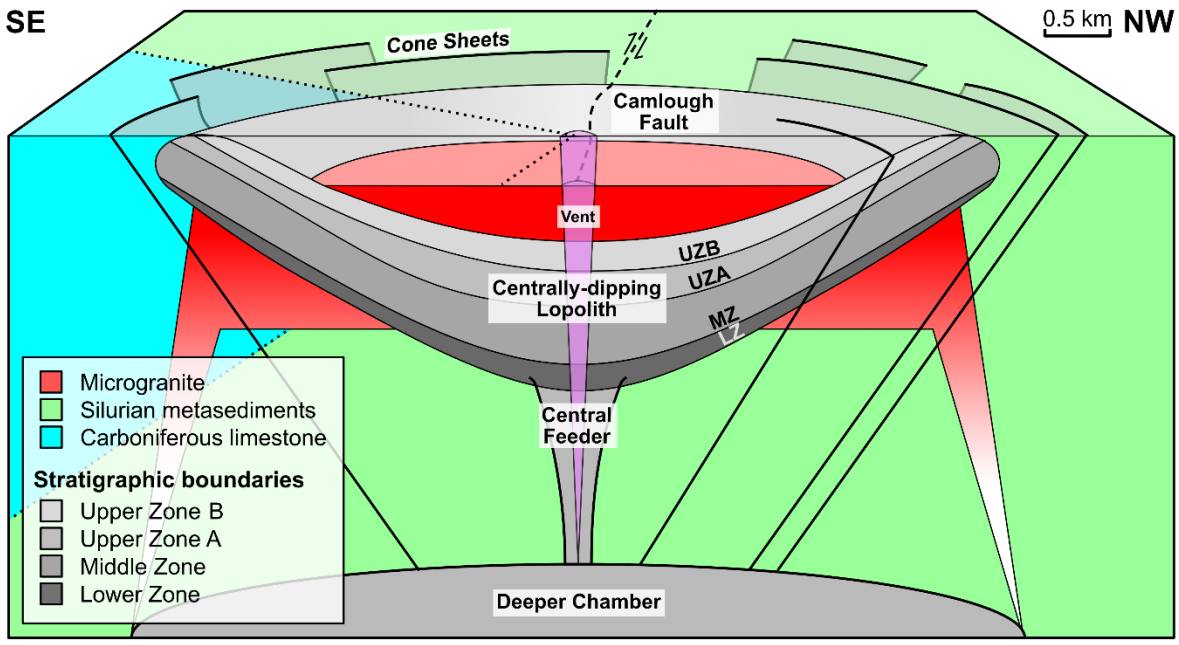

Figure 15: Idealised 3D model of the Carlingford Complex. Bimodal magmatism intrudes Silurian greywacke and Carboniferous limestone units along the Camlough fault (cf. Fig. 1b), interpreted as a potential feeder structure. Microgranite is emplaced as a ring dyke, whilst gabbro forms an inward-dipping lopolith (Buchanan, 1985, Meade, 2008, Meade *et al.*, 2014), consistent with magnetic susceptibility measurements (O'Driscoll, 2006), and our measurements of layering surfaces (Supplementary Table S3). Dolerite cone-sheets crosscut all major units and dip towards a central focus beneath the intrusion (Halsall, 1974, Schauroth *et al.*, 2014). They commonly entrain crystals, indicating a feeder reservoir beneath the layered gabbros, supported by geophysical surveys (Cook & Murphy, 1952, Hodgson & Young, 2016, Sajjadi *et al.*, 2020). Vent agglomerates postdate the intrusions and entrain all lithologies.

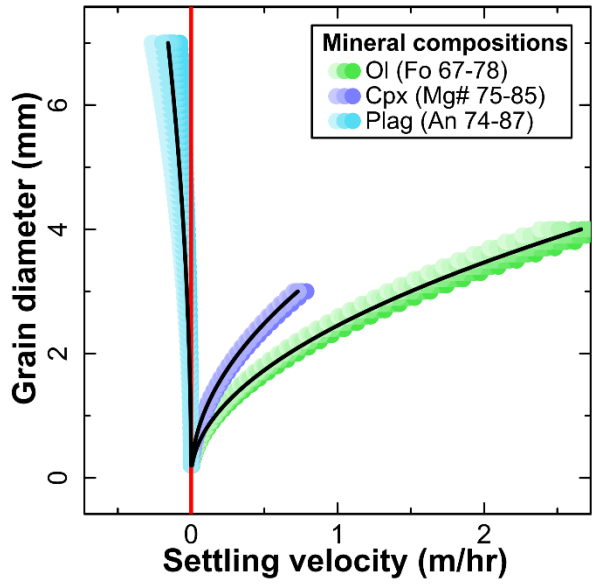

Figure 16: Stokes' settling velocities (Richardson & Zaki, 1954) calculated for the observed range in grain size and measured mineral core compositions (Supplementary Table S5) for olivine (green), clinopyroxene (purple), and plagioclase (blue). The liquid composition is taken as that of the most mafic aphyric cone sheet reported by Meade *et al.* (2014). Liquid density calculated via DensityX (Iacovino & Till, 2019). Liquid viscosity calculated following Giordano *et al.* (2008). Mineral densities calculated following (Robie *et al.*, 1967). Red vertical line = 0 m/hr settling velocity.

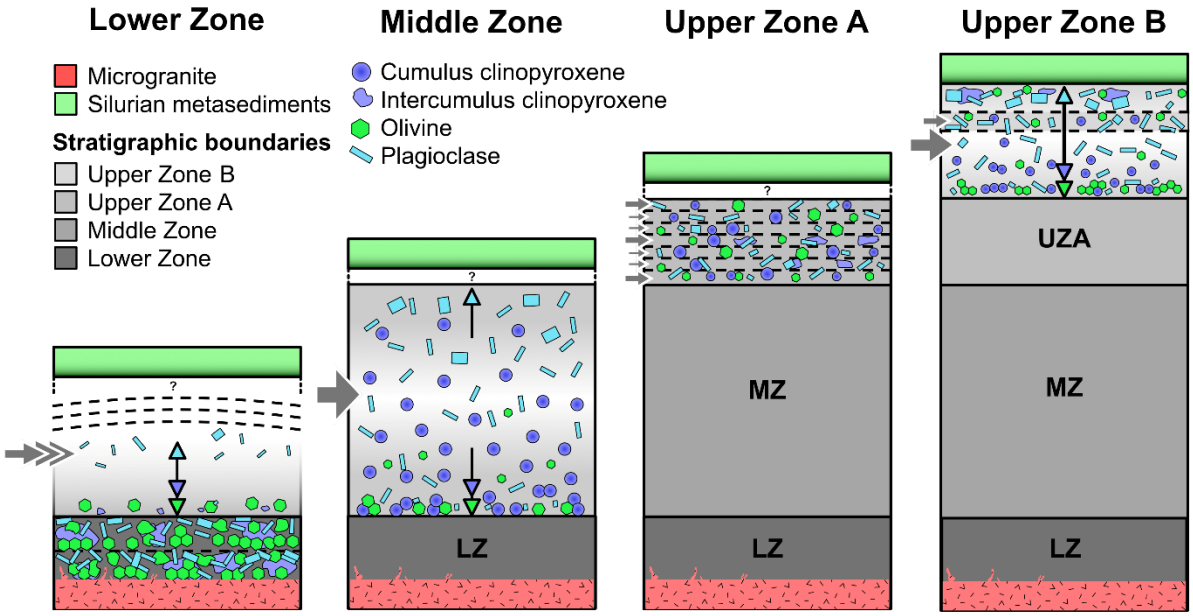

Figure 17: Schematic model showing the emplacement mechanisms for the four zones of the Carlingford Later Gabbros. Panels are arranged in stratigraphic order, though the actual emplacement sequence is uncertain (see text for discussion). **(a)** LZ: pulsed inflation of a liquid-rich chamber triggering punctuated settling into cyclic basal cumulates; **(b)** MZ: fractionation and crystal settling/flotation in a liquid-rich chamber producing intrusion-scale stratigraphic trends; **(c)** UZA: chaotic sill emplacement generating irregular stratigraphic trends; **(d)** UZB: combined liquid-solid intrusion and melt infiltration resulting in intrusion scale trends with localised disruptions. Light grey areas indicate relative melt volume; darker greys show solidified zones. Grey arrows denote magma flux; coloured arrows mineral settling/flotation (olivine = green; clinopyroxene = purple; plagioclase = blue). The question mark indicates the unknown upper intrusion contact, which is not exposed at Slieve Foye.

SUPPLEMENTARY FIGURES

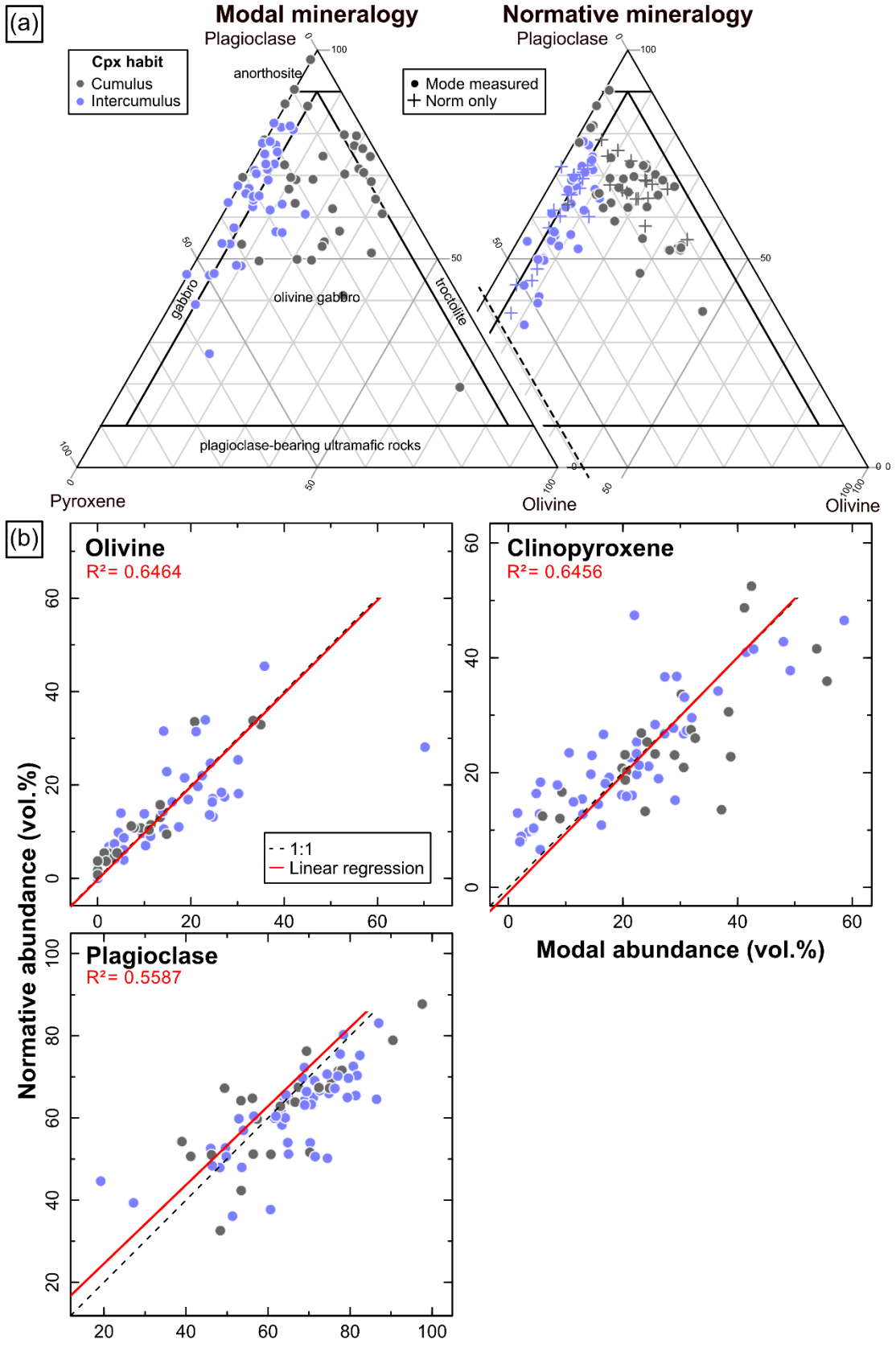

Figure S1. Comparison of measured modal and calculated CIPW normative mineralogy for Carlingford gabbros, with olivine, clinopyroxene, and clinopyroxene contents normalised to 100%. (a) IUGS ternary classification diagram for gabbroic rocks. (b) Scatter plots showing modal

vs normative abundances for each mineral phase. The full dataset is given in Supplementary Table S2.

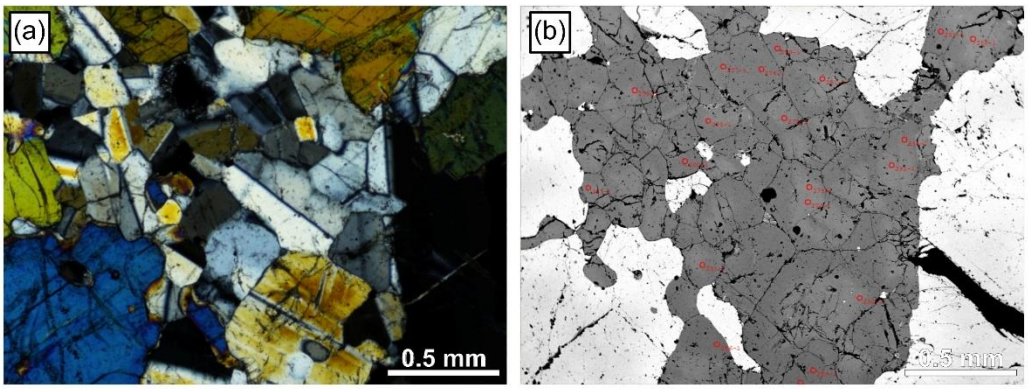

Figure S2. Aplite pipes/veins intruded into gabbros at South Foye Southern Flank. (a) *In situ* exposure of an aplite vein along its plane. (b) Loose block showing aplite veins of varying thicknesses.

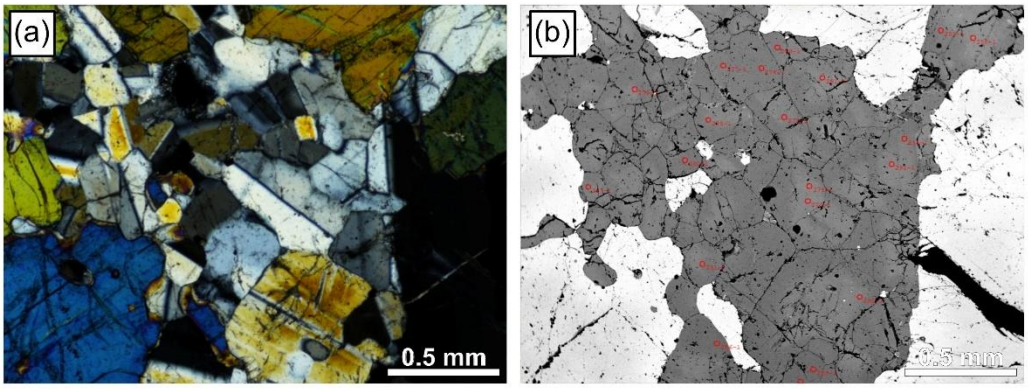

Figure S3. Well-sintered plagioclase aggregates displaying ~120° triple junctions (Sample 22CCCI2-02). (a) Cross-polarised light. (b) Backscattered electron (BSE) image.

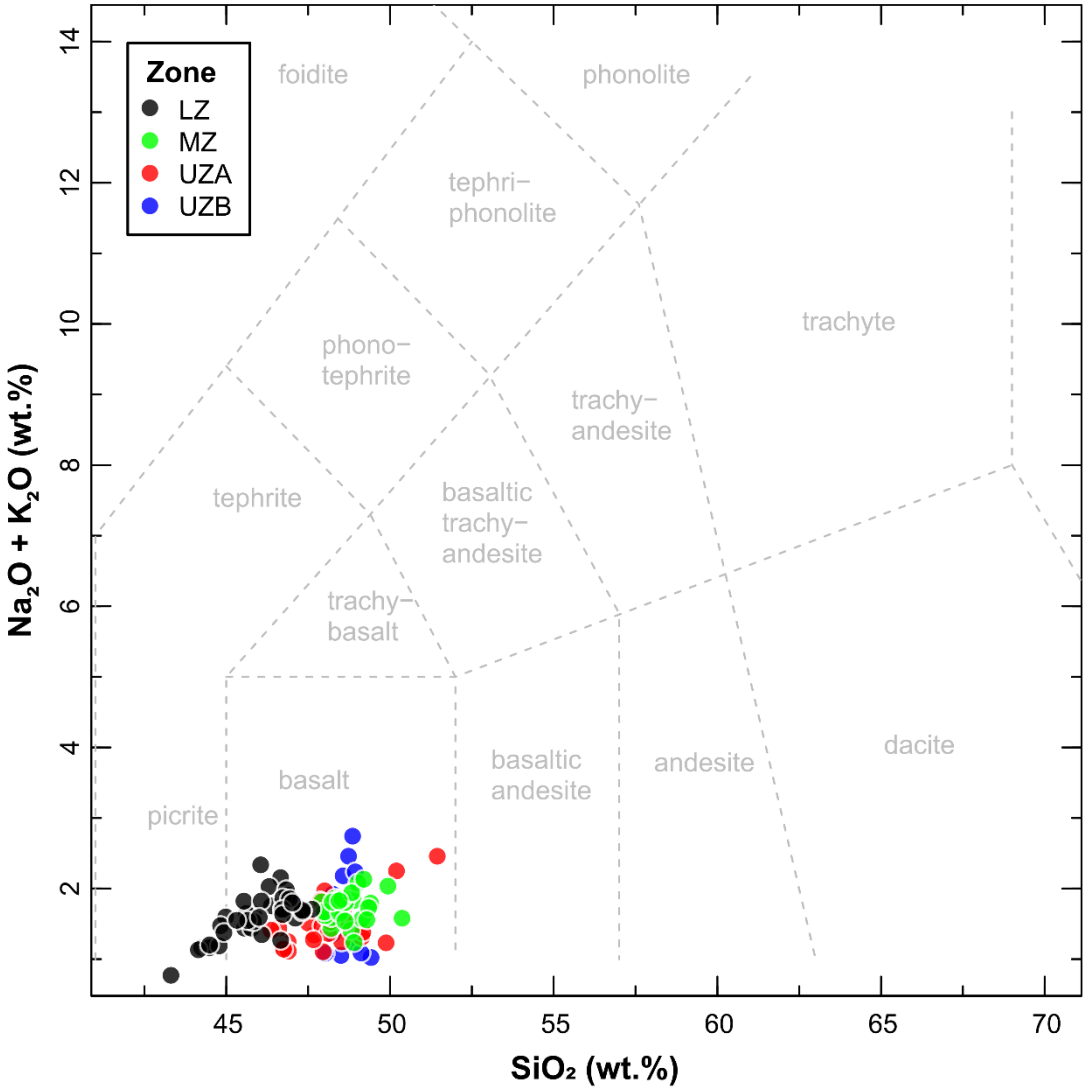

Figure S4. Total Alkali Silica plot showing chemical classification of the bulk rock samples. The full bulk rock XRF dataset is given in Supplementary Table S3.

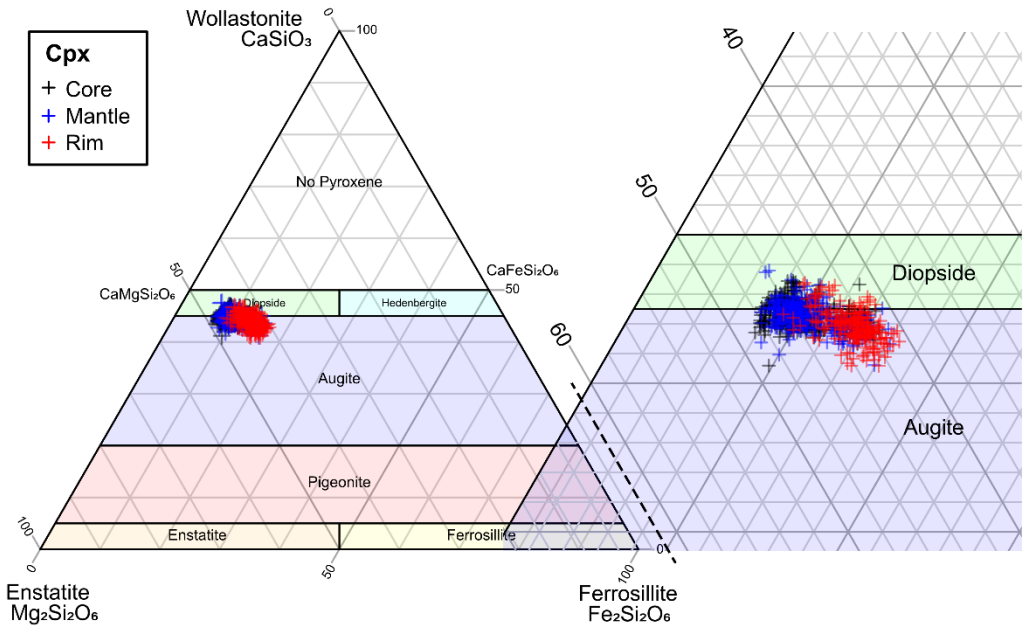

Figure S5. Pyroxene classification diagram summarising the measured pyroxene mineral compositions given in Supplementary Table S4.